Design of Resistivity Instrumentation for a He^3 Cryostat and its Application to the Charge Density Wave Superconductor Cu$_x$TiSe$_2$

by

Jason Iwachow

B.Sc., University of Waterloo, 2011

A THESIS SUBMITTED IN PARTIAL FULFILMENT OF
THE REQUIREMENTS FOR THE DEGREE OF

MASTER OF SCIENCE

in

The Faculty of Mathematics and Sciences
Department of Physics

BROCK UNIVERSITY
January 21, 2014

Abstract

Fermi patches in quasi-two dimensional charge density waves (CDW) have not described the connection to superconductivity (SC) according to theory adequately at this point in time. The connection between CDW and SC in the quasi-two dimensional material $Cu_x TiSe_2$ is an interesting one which might reveal mechanisms in unconventional superconductors. A previous Brock graduate student grew crystals of $Cu_x TiSe_2$. The precise doping of the samples was not known. In order to determine the doping parameter x in $Cu_x TiSe_2$, a sensitive resistivity measurement system was necessary. A new resistivity measurement system was designed and implemented utilizing an Infrared Labs HDL-10 He^3 cryostat. By comparing with data from the literature, doping of two samples was investigated using the new measurement system and a Quantum Design Magnetic Property Measurement System (MPMS). Methods for determining the doping revealed that the old resistivity system would not be able to determine the CDW transition temperature of highly doped samples or doping for elongated samples due to electronic noise. Doping in one sample was found to be between x=0.06 and x=0.065. Values of doping in the second sample had a discrepancy but could be explained by incorrect sample

orientation.

Contents

Glossary

AC   Alternating Current

API   Application Programming Interface

BCS   J. Bardeen, L. N. Cooper, and J.R. Schrieffer Theory of Superconductivitiy

CDW   Charge Density Wave(s)

DC   Direct Current

EMF   Electromotive force

GPIB   General Purpose Interface Bus, specified by the IEEE-488 standard

IC SIP   Integrated Circuit Single Inline Package

MPMS   Quantum Design Magnetic Property Measurement System

RF   Radio frequncy, specifically electromagnetic waves in the radio spectrum

RMS   Root Mean Squared

SC   Superconductivity

SQUID   Superconducting Quantum Interference Device

VDP   Van der Pauw

List of Figures

Acknowledgements

Dr. Maureen Reedyk

    For her stress free guidance throughout my studies

Xiao Peng and Yang Pan

    For introducing me to the instruments in the lab when I was new to Brock University

Jason Manson

    For his help in theoretical concepts and with experimental debugging

And to my wife, Megan

    For her constant support and understanding during those months of perpetual work.

1. Introduction

Superconductivity (SC) had been theorized to come about by electron electron inter-actions in 1957 by Bardeen, Cooper, and Schrieffer (BCS) [1]. A similar phenomena, the charge density wave (CDW), was postulated to exist by Frölich in 1954 based on electron hole interactions [2]. These two phenomena are quite similar in principle but the CDW leads to an insulating condensate because the pair is charge neutral while in SC the pair has a charge of 2e. The theory behind CDW requires that the system is quasi-one-dimensional in order for the electron hole pairs to cause the Lindhard response function to diverge around $\pm k_f$, a process called nesting [3]. In 1974 it was discovered that anomalous properties of $TaSe_2$ and TaS_2, which are quasi 2D systems, are due to CDW's [4]. $Cu_x TiSe_2$ is also a quasi-two-dimensional material which exhibits the CDW state [5]. $Cu_x TiSe_2$ also exhibits a superconducting phase that has a varying Tc based on the doping (parameter x) which seems to take over the CDW state. D. W. Shen et al. [6] discuss the possibility that flat portions at the Fermi energy in two dimensions in the first Brillouin zone can allow for such nesting (called Fermi patches) to occur for three directions in the a-b plane [6]. However, theory still fails to explain why CDW's appear

to compete with SC states, the phase diagram of the material, or why an anisotropic gap can occur for SC when BCS predicts an isotropic gap [7]. The connection between SC and CDW is of valuable interest in seeking the answers to the problems associated with understanding unconventional superconductors.

Measurements on the previous resistivity measurement system were too noisy to determine the CDW transition temperature in crystals of Cu_xTiSe_2. In order to make investigations of the properties of Cu_xTiSe_2, it was necessary to construct a resistivity measurement system which could accurately measure the resistivity to detect the transition in and out of the CDW state as well as the SC transition. This system has been realized and utilized to determine the doping concentration x in Cu_xTiSe_2 which was not possible before. Noisy measurement systems require stronger applied currents which affect the values that are of interest. The previous system, based on Infrared Lab's HDL-10 He^3 Cryostat, that was intended for optical measurements, was adapted haphazardly by previous graduate students with little attention to noise protection in the system. Additional measurement capabilities which were lacking on the previous design were also incorporated. Measurement of multiple samples was implemented which conserves liquid helium and time. The Hall effect measurement capability was also introduced with the new design, and could be used to probe the charge of the carriers; thus probe for a CDW transition [5].
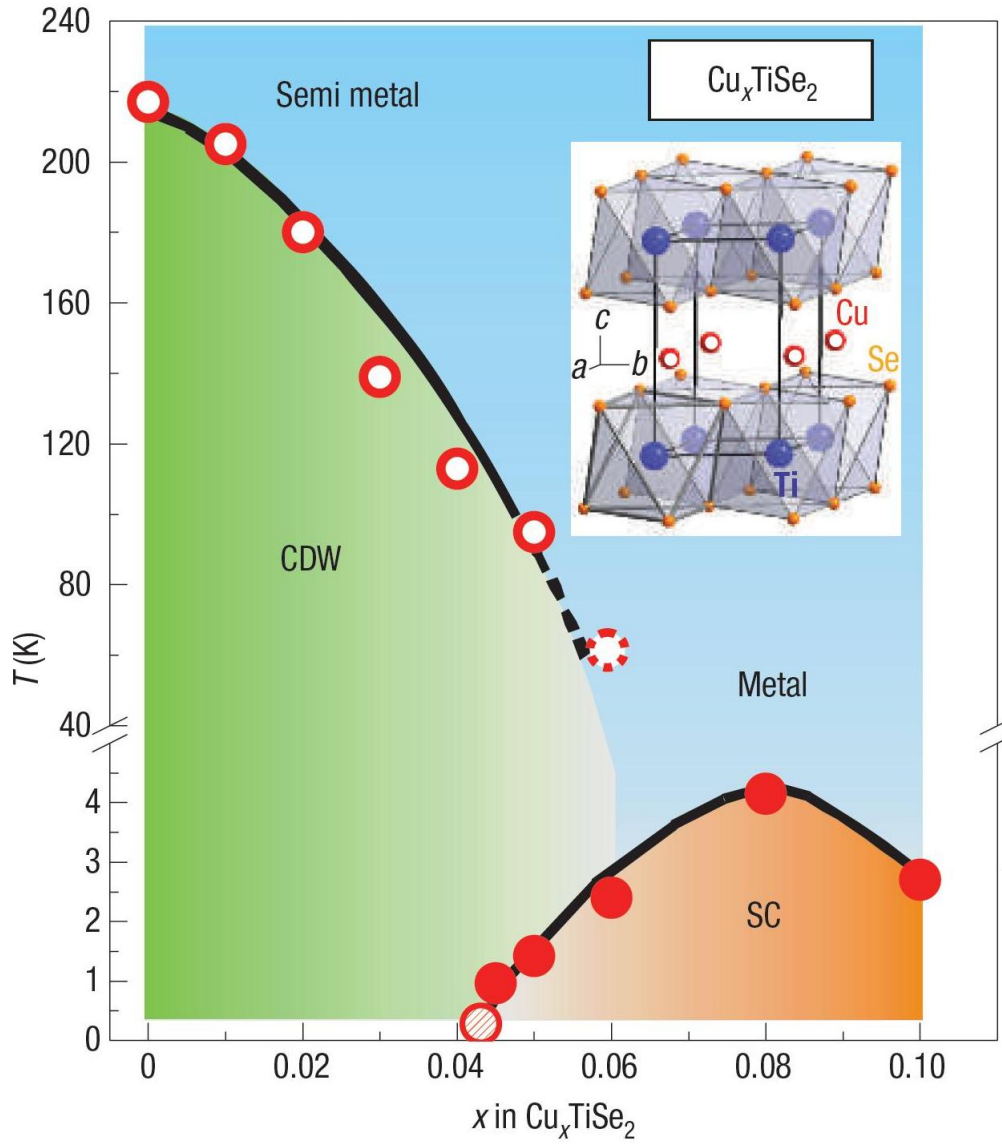
Figure 1.1.: The phase diagram of Cu_xTiSe_2. Shows as doping of copper increases, CDW disappears in favor of SC states. Note that there is a region of coexistence. The inset is the crystal lattice of Cu_xTiSe_2. Reproduced from [5].

1.1. Crystal structure of Cu$_x$TiSe$_2$

The undoped crystal structure of TiSe$_2$ belongs to a group of materials called chalco-genides, with the generic formula MT$_2$. M is a transition metal and T is a chalcogen anion S, Se, or Te. They usually have one of two crystal structures, designated either 1T or 2H phase [8]. Chalcogenides are layered compounds where the layers are held together by van der Waals forces. In the 1T phase, the Ti atoms are in octahedral coordination with Se, shown in Figure 1.2 b), to produce a trigonal octahedral crystal (shown in inset of Figure 1.1. The layers X' and X are the chalcogens and M is the transition metal. The layers X and X' are two-dimensional hexagonal lattices where the X' layer is parallel and rotated 60 degrees relative to the X layer. In the 2H phase the layers are stacked (using notation from Figure 1.2) X'MX' XMX instead of X'MX X'MX, producing a trigonal prismatic structure.

TiSe$_2$ takes on the 1T phase. It is between the layers, the area held together by the van der Waals force, that the copper dopant is intercalated causing expansion of the unit cell in the a and c direction. This expansion is linear until it becomes constant for dopant concentration x$\geq$0.11 [5]. The structure shows clear quasi-two-dimensionality, and this results in a quasi-two-dimensional CDW. The CDW in two dimensions occurs by nesting on flat portions, called "Fermi patches" at the Fermi energy in the first Brillouin zone [5]. As an example, Figure 1.3 shows the 2D Fermi patches in the joint density of states of 2H-Na$_x$TaS$_2$, another superconducting CDW material. The van der Waals forces are weak compared to the bonding in the crystal which makes determination of the orientation of the crystal for this material relatively easy by the rough method of
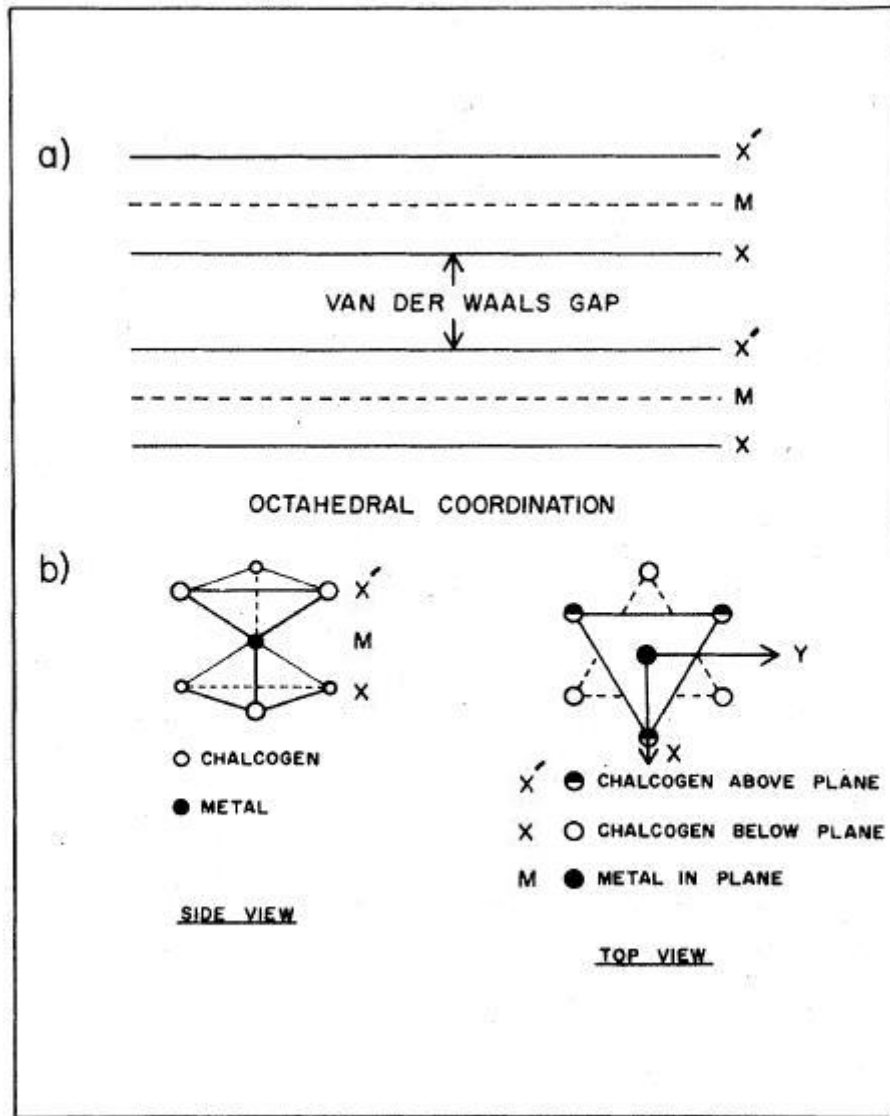
Figure 1.2.: Crystal structure of $1T$-TiSe$_2$. a) Cross sectional view of the lattice layers showing relative positions. Layers X' and X are chalcogen atoms and M is the transition metal b) Octahedral form of the $1T$ phase of the lattice where the chalcogen is Selenium and the metal is Titanium. Reproduced from [9].
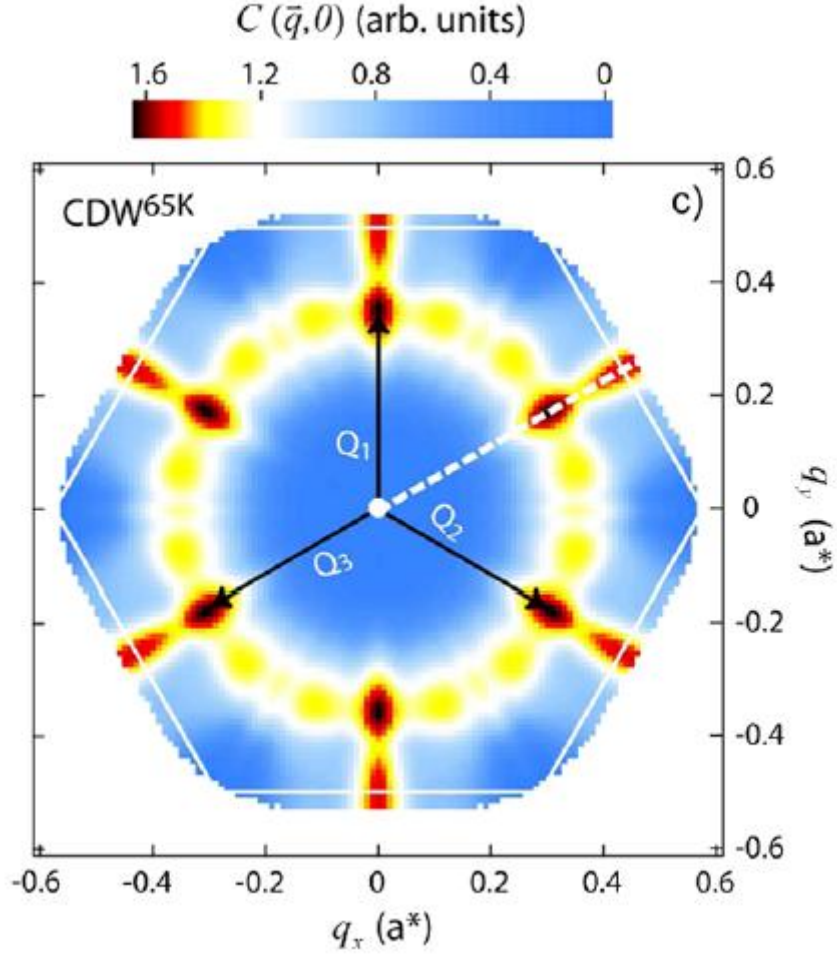
Figure 1.3.: Joint density of states in 2D momentum space of the two dimensional superconducting (T_c=2.3K) CDW (T_{CDW}=65K) material $2H$-Na$_x$TaS$_2$ in the CDW state. The CDWs are situated on the high density patches in three directions $\vec{Q}_1$, $\vec{Q}_2$ and $\vec{Q}_3$. Reproduced from [6].

checking the plane which is easiest to cleave. This will be parallel to the a-b plane.

1.2. Sample Preparation

Batches of single Cu_xTiSe_2 crystals were grown by Artorix de la Cruz de Ona at Brock University using the iodine-vapour transport method as described by Wu et. al. [8]. Large crystals were selected to be able to conduct measurements easily and for future optical spectroscopy research that yields stronger signals for larger reflective sample surfaces. Two large single crystal samples were selected to be measured. Sample 1 was the largest out of these and is shown in Figure 1.4. Sample 2 is elongated and shows the silver paint contacts to be quite close to each other on either end of the sample as seen in Figure 1.5. Both Figures 1.4 and 1.5 show the silver paint contacts for resistivity measurement whose dimensions can be seen to be a significant fraction of the distance between contacts. The consequences of this will be discussed later in section 2.2.1.
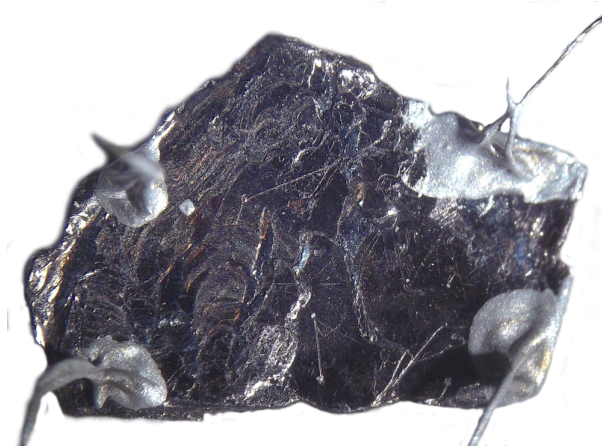
Figure 1.4.: Photograph of Sample 1 taken under a microscope. The background was erased to show the boundaries of the crystal clearly. Four gold wire silver paint contacts are on the perimeter of the sample. Largest dimensions of the sample are 6.0 mm along its length (oriented horizontally in the figure), 4.1mm along its width (oriented vertically in the figure) and 0.344mm in thickness.
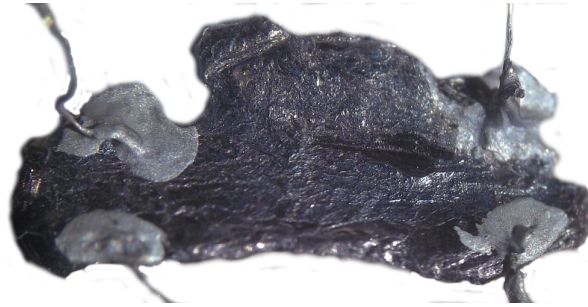
Figure 1.5.: Photograph of Sample 2 taken under a microscope. The background was erased to show the boundaries of the crystal clearly. Four gold wire silver paint contacts are on the perimeter of the sample. Largest dimensions of the sample are 6.9 mm along its length (oriented horizontally in the figure), 3.0mm along its width (oriented vertically in the figure) and 0.700mm in thickness.

2. Instrumentation

A resistivity measurement system was greatly improved upon and further developed in order to conduct more accurate and reliable measurements. The original set up consisted of nano volt meter, nano current source, actuator switch connected into the cryostat through various connection boxes, where the instruments were controlled with GPIB (IEEE488) through a macro for the MPMS MultiVu program. The distribution box for connections into the cryostat was made by Infrared Labs.

An input line was used for setup conditions and data was recorded to a file which MultiVu reported. This original resistivity instrumentation produced noisy results due to the system being unshielded and cluttered by redundant and insecure connections. The software implementation was also crude and gave little information to the details of the measurement and no chance of diagnosing problems. Noise levels were on the order of 15 nV$_{RMS}$. Contributions to this noise were from the instruments, Nyquist noise, magnetic and RF sources. The new system implementation has reduced noise in the system by a factor of 3.

2.1. Principle

Instrumentation was designed to implement multiple sample resistivity or Hall effect measurements by the van der Pauw method. In 1958 L. J. van der Pauw showed that resistivity or the Hall coefficient of an arbitrary shape can be measured by a four contact measurement if the sample is thin and of uniform thickness, contacts are small, contacts are on the circumference, and the sample contain no holes [10]. Consider the arbitrary shaped sample of small uniform thickness in Figure 2.1.
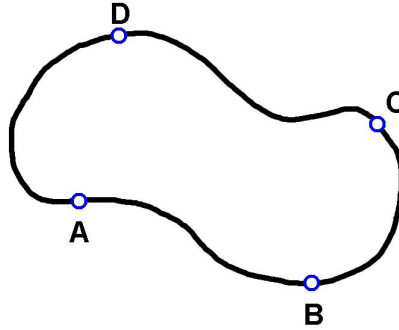
Figure 2.1.: Top view of an arbitrary shape of uniform thickness with point contacts labeled A,B,C, and D which can be used with the van der Pauw method.

If we apply a current to A (positive) and B (negative), I_{AB}, and measure the voltage at D (positive) and C (negative), V_{DC}, then we can define the resistance:

$$R_{AB,DC} = \frac{V_{DC}}{I_{AB}}$$

We can call this resistance measurement the "horizontal" configuration. Similarly for current on B,C and voltage reading on A,D gives $R_{AD,BC}$ (similarly called the "vertical"

configuration), then the resistivity of the sample can be shown [10] to be:

$$e^{\frac{-\pi R_{AB,DC}d}{\rho}} + e^{\frac{-\pi R_{AD,BC}d}{\rho}} = 1 \qquad (2.1)$$

Where ρ is the resistivity of the material and d is the thickness. There is practical further improvement to this measurement. By reversing the current in each configuration and taking the average of each, any DC offset present in the system can be canceled out. Taking the averages for the resistances in their respective configurations:

$$R_{horz} = \frac{R_{AB,DC} - R_{BA,DC}}{2}$$

$$R_{vert} = \frac{R_{AD,BC} - R_{DA,BC}}{2}$$

Gives us a more reliable value for those resistances. Equation 2.1 becomes

$$e^{\frac{-\pi R_{horz}d}{\rho}} + e^{\frac{-\pi R_{vert}d}{\rho}} = 1 \qquad (2.2)$$

A Hall effect measurement using the setup to be described can be done by applying current on A,C and measuring the voltage change on D,B as a uniform magnetic field is applied perpendicularly to the surface and then reversed in direction [11]:

$$R_H = \frac{d \cdot \Delta V_{DB}}{B \cdot I_{AC}} \qquad (2.3)$$

Where R_H is the Hall coefficient and B is the magnitude of the magnetic field[1].

_____

[1]not to be confused with the subscript B which represents the contact across which the voltage is being measured.

2.2. Measurement Noise

There were many different sources of noise that entered the system before it was improved. Noise levels prevent accurate measurements. Noise can drown out important characteristics in data, reduce resolution and prevent valuable measurements of very low resistance materials. In the work carried out for this thesis, sources of electromagnetic noise that were present in the system were suppressed using standard engineering practices. Noise is typically measured in root mean squared (RMS) values of voltage and power. The root mean squared value can be calculated for a set of data x_n in the following way:

$$x_{rms} = \sqrt{\frac{1}{n} \sum_{0}^{n} (x_n - \bar{x})^2} \tag{2.4}$$

Where $\bar{x}$ is the base line signal value. The noise that is of importance to the measurement of resistivity is the noise associated with the voltage measurement.

2.2.1. Contact Problems

The van der Pauw method assumes that the contacts are very small compared to the sample size and they occur at the circumference of the material. When measuring a sample which is less than about 0.5mm in its largest dimension, the contact size becomes a problem.

The estimation of error [11] in resistivity $\Delta\rho$ deviating from the true value ρ for a length along the circumference l (Figure 2.2 a), a strip length l of contact from the circumference (Figure 2.2 b), or a contact a distance l away from the circumference

(Figure 2.2 c) for a circular sample of diameter ø causes an error on the order of

$$\frac{\Delta\rho}{\rho} \sim \frac{-l^2}{\text{ø}^2 \ln(2)}$$
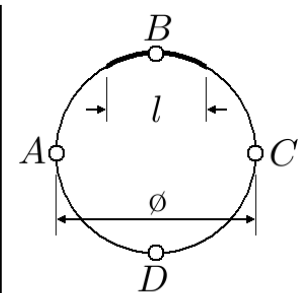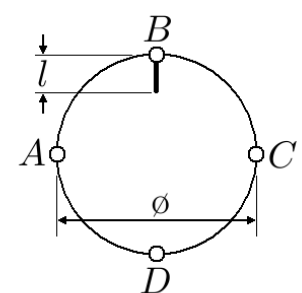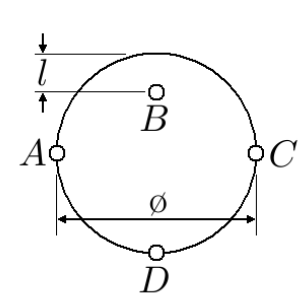
$\frac{\Delta\rho}{\rho}$	a)	b)	c)
	$\approx \dfrac{-l^2}{16\text{ø}^2 \ln 2}$	$\approx \dfrac{-l^2}{4\text{ø}^2 \ln 2}$	$\approx \dfrac{-l^2}{2\text{ø}^2 \ln 2}$

Figure 2.2.: Errors with the van der Pauw method associated with different imperfect contact types. Reproduced from [11].

This error becomes quite large when the distance between contacts approaches the size of the contact. The other problem that arises for small samples is when the sample is elongated, such that contacts A,B and C,D are very close while each pair are far from each other. This causes the horizontal configuration to have high noise since the electric field that extends to C,D is weak; thus the voltage measured is very low and then other sources of noise which are independent of signal amplitude start to dominate while the vertical configuration will yield a higher voltage. If the sample is sufficiently long[2] then

---

[2]When $L_{A,D} \gg L_{A,B}$ the van der Pauw derivation is no longer valid for finite contact size.

the resistivity can be approximated to that of a two contact measurement with four leads.

2.2.2. Instrument Noise

In reality instruments for measurement never meet the ideal case which is discussed in theory. In the case of a voltmeter, it ideally has infinite impedance and measures the voltage exactly without noise. However, in order to do a measurement of voltage, some current must be drawn and thus presents a finite impedance. Even more problematic, measurement devices involve their own circuitry that introduces its own sources of noise, in particular thermal agitation noise in transistors. This sets a lower bound on the noise level that can be achieved. Noise levels are usually given by the manufacturer in the specifications, however in this thesis work they were measured to confirm them and identify other sources of noise.

2.2.3. Nyquist Noise

Nyquist noise, discovered by Johnson in 1928 [12] is noise that arises in a circuit due to charge carriers in thermal equilibrium, which are in a state of permanent thermal agitation [13]. Nyquist noise is voltage fluctuations that occur (on average) uniformly over the whole frequency spectrum[3], called white noise [13]. The equation is given by:

$$V_{RMS} = \sqrt{4k_B T R \Delta f} \tag{2.5}$$

---

[3]The spectral density of Nyquist noise is constant up to the angular frequency corresponding with the correlation time $\sim 10^{14} s^{-1}$, see bibliography entry [13].

Where V_{RMS} is the RMS noise of the voltage in the conductor in the frequency bandwidth Δf, R is the resistance in ohms, T is the temperature in Kelvin and k_B is the Boltzmann constant [14]. We are interested in making DC measurements and ideally the bandwidth is zero, but no DC measurement is purely DC since there is always a time range of measurement which sets the bandwidth. Therefore, the noise that arises in the measurement from Nyquist noise is unavoidable at some level since the measurement is always carried out at finite temperature. This means that the measurement leads and the material that is being measured are likely to contribute the most Nyquist noise.

2.2.4. Thermoelectric Effects

Thermoelectric generation effects occur when there is a temperature difference across two contacts in a circuit that are made of different conductors (specifically with different Seebeck Coefficients). Thermoelectric voltages are generated when there is an electrochemical potential in the circuit and are created by a thermal gradient [13]. The voltage generated is defined as

$$E_{emf} = -S\Delta T \tag{2.6}$$

where S is the Seebeck coefficient and ΔT is the difference in temperature between the contacts [15]. In order to cancel these effects for equilibrium conditions resistance is measured by applying current in both directions and averaging the results. However, these effects can have an impact on the measurement while temperature is changing. The time dependent version of the Seebeck equation (equation 2.6) for a delay τ in

measuring positive and negative current is given by:

$$V = -S \int_0^\tau \Delta \frac{dT}{dt} dt \approx -S\Delta\frac{dT}{dt}\tau \tag{2.7}$$

In the Infrared Labs HDL-10 He^3 cryostat (henceforth to be referred to as "the cryostat"), the largest Seebeck coefficient difference of any signal carrying wires is 40 μV/K (Constantan and Copper at room temperature). If we estimate that the rate of cooling is 0.2 K/s, and modestly estimate the Leidenfrost point for liquid nitrogen is 277K in the cryostat[4], we obtain a value of a time dependent thermoelectric voltage of about 16mV. This is highly significant for materials being measured with very low currents or very low resistivities. However, for warm up times that take days this value is on the order of 10^{-10} V. This means that cool down measurements are very untrustworthy while for warm up measurements this is a very minimal contribution to measurement signal disturbance.

2.2.5. Electromagnetic Noise

The environment has many sources of magnetic fields, electric fields and electromagnetic fields. Radio frequency (RF) noise is naturally present in the environment and is easiest to reduce. RF noise comes from space, man made sources for telecommunication, as well as from undesired radiation sources such as paired signal lines that have bends, terminations or discontinuities [16]. These sources that are present in the environment, present a source of noise in the lab by absorption into signal transmission lines that are not properly shielded. RF noise can be effectively removed from the system by "wrapping"

---

[4]The rate of cooling is greatest below the Leidenfrost point because there is no insulating vapor blanket.

all of the signal lines used with a conductor that is grounded. This grounded shield prevents signals entering the system by acting as a reflector and Faraday cage. This blocks both RF signals and electrostatic fields. A coaxial cable is a typical example of the implementation of this idea, and is used in this resistivity measurement system. Magnetic noise, however, is more difficult to block. Slowly varying magnetic fields such as those from an AC power distribution[5], the Earth, or a vibrating ferromagnetic material will penetrate Faraday cages. A straight transmission pair will have a gap between the conductors, and if a varying magnetic field is present, the flux through that area will induce a voltage. One solution to this problem is to surround the signal lines with a high permeability material to "redirect" the field lines away from the signal lines, an example product being MuMetal [17]. The magnetic field does not need to be zero inside this region; there is an alternative solution.

Consider a transmission line that consists of two twisted wires as shown in Figure 2.3 a). If we assume the source of the varying magnetic field to be sufficiently far so that the field is almost uniform around the twisted pair, and the twists to be approximately the same spacing, then for any direction of the magnetic field the flux in each twist will be equal and opposite to adjacent ones. This will cause an EMF to be induced in equal yet opposite directions and therefore cancel out, shown in Figure 2.3 b). Cables using twisted pairs inside a braided metal sleeve that is grounded remove most of both RF and slowly varying magnetic fields. This is implemented everywhere possible in the resistivity system that was designed for this thesis work.

---

[5]Referring to power for buildings in north America $120V_{RMS}$ at 60Hz.
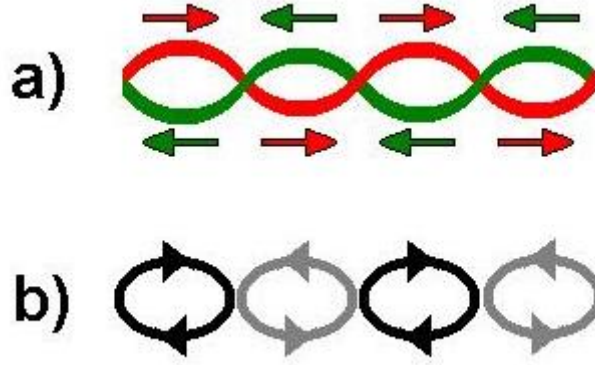
Figure 2.3.: a) Two insulated conductors twisted together to form a twisted pair signal line. The arrows indicate an example for the direction of the current. b) shows how the twists create spaces of opposite vector areas such that the induction in one twist is canceled out by the next for a magnetic field spatially uniform in that region. Reproduced from [18]

2.3. Design and Method

The instrument design consisted of three basic components. The sample was mounted on a holder inside the Infrared Labs HDL-10 He^3 cryostat. The connections led to a 32 pin connector that in turn led to the distribution box where the instruments were connected. The information from the instruments was then read through IEEE-488 (known as GPIB) communication to the computer where the data was collected in the resistivity program.

2.3.1. The Cryostat

The cryostat is where the sample resides and which provides an environment that can potentially reach temperatures of ~ 0.4 degrees Kelvin. The sample holder is mounted on either the bolometer stage or sample stage (see Figure 2.4). Spare connections inside the cryostat were utilized for resistivity connections by installing 6 pin IC SIP plugs. Once the sample holder is mounted and plugged in, the cryostat is sealed and evacuated to pressures on the order of $1 \cdot 10^{-6}$ Torr. Thermal radiation shielding is maintained by filling the shield vessel (nitrogen vessel that is thermally connected with the shield) with liquid nitrogen. Cooling is achieved by filling the main vessel (helium vessel which is thermally connected with the cold plate) with liquid nitrogen first. This is then replaced with liquid He^4. Liquid Nitrogen precooling reduces liquid helium boil off during the transfer. Evacuating the vessel (pumping) can lower the temperature to $\sim$ 2K, below which then the He^3 one shot refrigerator is utilized to go to as low as ~ 0.4 degrees Kelvin. He^3 refrigeration is achieved by the following steps. The He^3 tank is connected through a valve to a charcoal pump. The He^3 tank valve is opened, allowing absorption of He^3 in the charcoal pump at the He^4 boiling point. A thermal switch is opened to thermally isolate the pump from the cold plate and sample, and the He^3 tank valve is closed trapping the He^3 gas. Heat is applied to the charcoal pump to raise its temperature. The power is turned off at around 40K, and the thermal switch to the stage where the sample holder is mounted is closed, allowing the He^3 vapour to condense in a vessel thermally connected to the stage on which the sample holder is mounted cooling it to as low as ~ 0.4K when the charcoal pump is cooled to allow it to pump on the
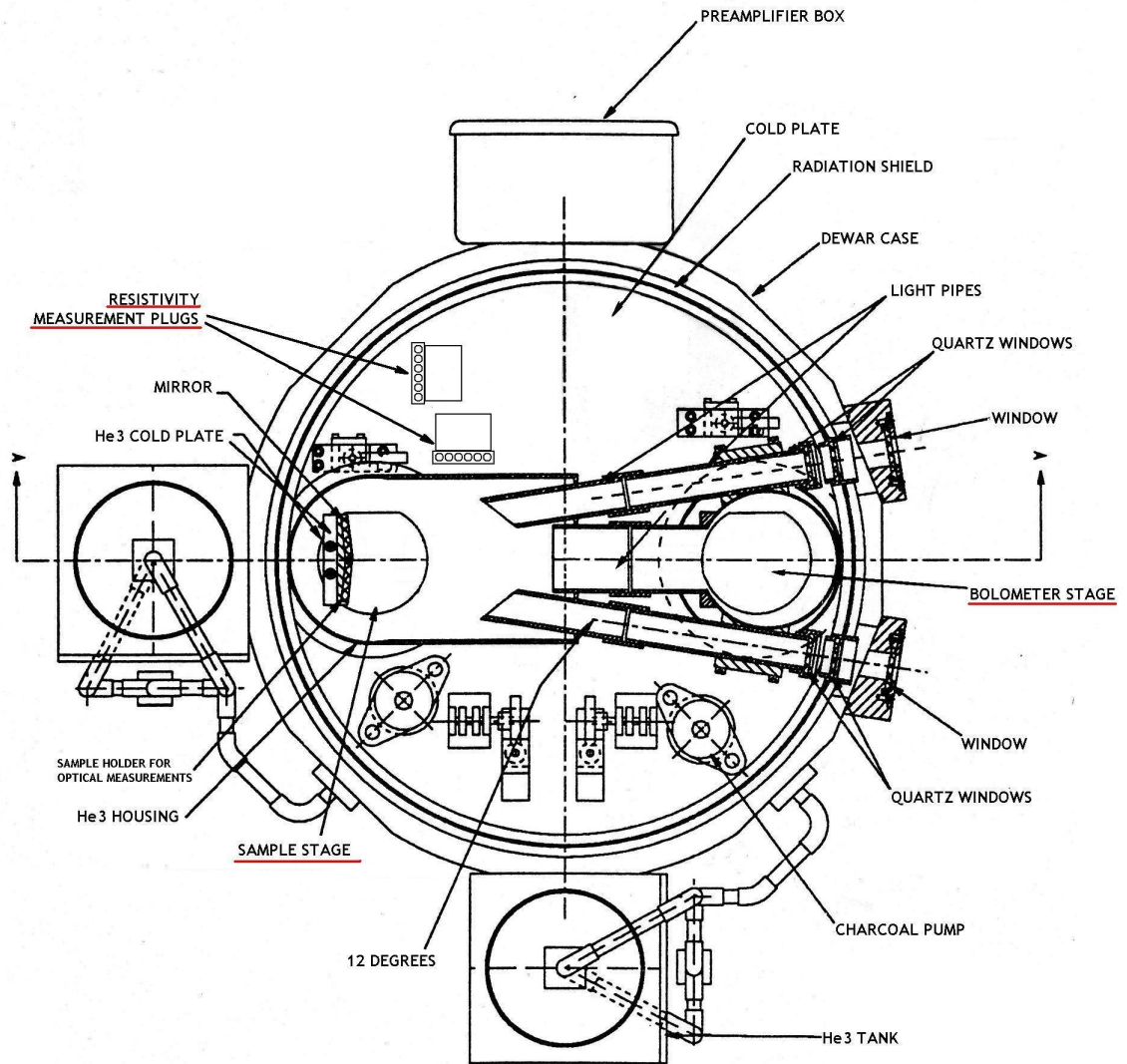
Figure 2.4.: The schematic of the Infrared Labs HDL-10 He^3 cryostat. Modified from [19]. Sample holder was mounted on the bolometer stage.

condensed He[3]. Temperature is not maintained at any point other than at the boiling points of N_2 and He[4]. Temperature dependent data is taken by letting the system warm up at its own pace. With the system evacuated and the thermal shield vessel depleted[6] typical warm up times from 4 K to 300 K are on the order of 72 hours.

2.3.2. Sample holder

The sample holder was constructed to make mounting of samples easily interchangeable. Figure 2.5 shows one empty sample holder. Samples are either glued with GC varnish, epoxy or double sided tape into positions A and C. Gold wire is soldered to the copper wires around those positions and the other end is made into a contact on the sample using silver paint. Copper wires around the sample positions are placed so that orientation of the contacts is unambiguous.

    In the center, at position B, there is a Lakeshore DT-670 silicon diode temperature sensor mounted to measure temperature for temperatures between 1.4 K - 500 K. There are three temperature sensors built into the cryostat; Two sensors at the sample stage (a B sensor for high temperature and an A sensor for low temperatures) and one in the bolometer stage (an A sensor for low temperature). Two sensors are used to accurately measure the full range of temperatures in the experiment (see section 2.3.3). In the sample holder shown in Figure 2.5, the temperature sensor at position B is used as the B sensor for the temperature controller. The bolometer stage has no sensor for

---

[6]If the shield is not depleted thermal equilibrium will be maintained at the boiling point of liquid nitrogen
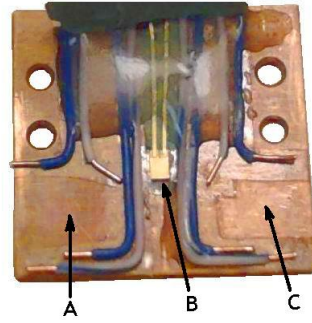
Figure 2.5.: The sample holder that is used inside the cryostat. Samples are mounted

with glue onto the copper plate at positions A and C. Sample one is at A

and sample two is at C. At position B there is a Lakeshore DT-670 silicon

diode temperature sensor mounted with indium solder. Used as the B sensor

in the temperture controller. (see main text at sections 2.3.2 and 2.3.3)

the temperature range 6 K - 500 K. Mounting the temperature sensor directly on the

sample holder has the additional benefit of reducing error associate with reading the

temperature in thermal non-equilibrium for a temperature gradient between the sample

and the sensor.

2.3.3. Measuring Circuit

The block diagram of the measuring instrument circuit is shown in Figure 2.6. The

32 pin connector from the cryostat goes into the distribution box which breaks out to

all the instruments. The temperature is measured through the Lakeshore DRC-91CA

temperature controller, which contains the data for the voltage - temperature curves.

It has two inputs, one for sensor A (the low temperature sensor) and one for B (the

high temperature sensor). The distribution box has a switch to control which A and B sensor to read from, either bolometer or sample stage. The B sensor mounted within the cryostat (the Lakeshore DT-470 silicon diode sensor) is only accurate to 6 K. The A sensor (the Lakeshore GR200A germanium sensor) is accurate below this temperature to about 0.3 K. With the DT-670 sensor used as the B sensor, the switch from A to B sensor occurs at 1.4 K.

An HP 34420A nano volt meter and Keithley 6221 DC and AC current source are connected with a 4 pin mini XLR cable utilizing the noise reduction methods described earlier to the HP 34970A data acquisition/switch unit with an HP 34903A 20 channel actuator general purpose switch card. The HP 34903A card in the switch unit allows for the voltage (V+, V-) and current source (I+, I-) contacts to be arranged in any permutation to the contacts A,B,C, and D on sample A or B. This allows for not only resistivity measurements but also Hall effect measurements. From the switch unit, two 4 pin mini XLR cables, each representing the four contacts from one sample, are connected to the distribution box. The three voltage sources in Figure 2.6 are connected to the distribution box by BNC coaxial cables. These are power supply equipment that were made at Brock University's Electronics Shop. They manually control power to the bolometer stage charcoal pump, sample stage charcoal pump, and cold plate heater. An HP 34401A Multimeter is used to measure the resistance of the charcoal pumps, giving a rough estimation of its temperature. A switch on the distribution box controls which stage it is measuring.
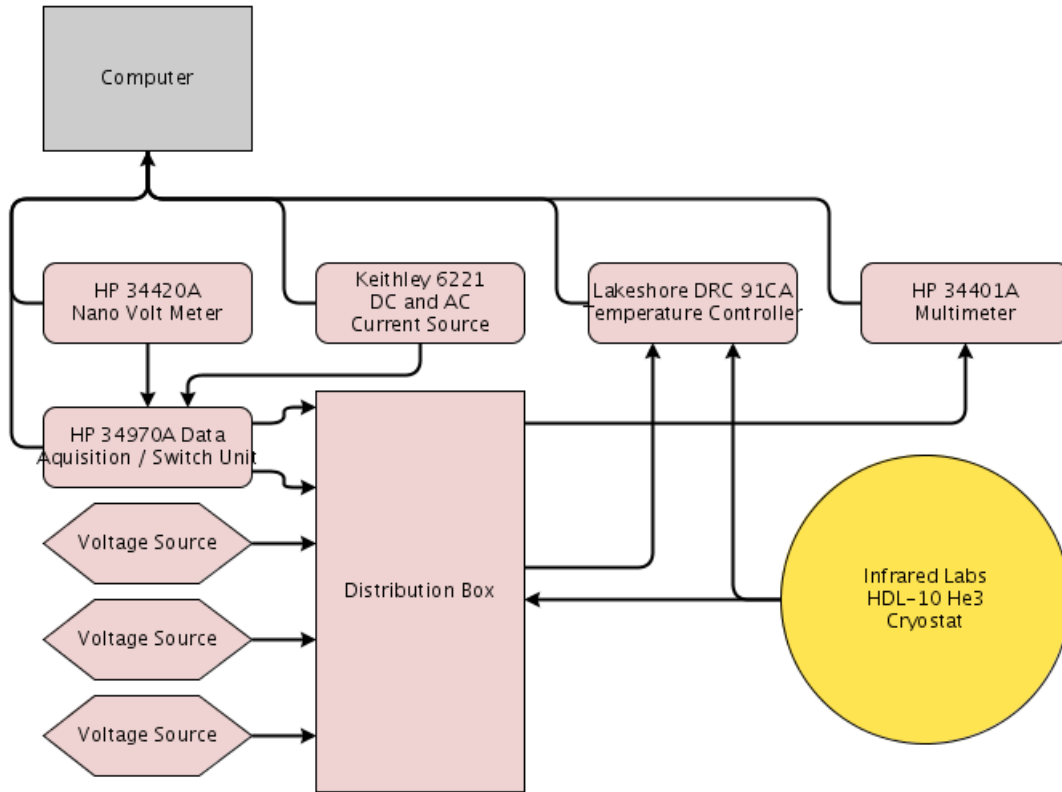
Figure 2.6.: The block diagram of the resistivity setup. Voltage sources specified are power supply equipment that were made at Brock University's Electronics Shop. The HP 34970A data acquisition switch unit utilized an HP 34903A 20 channel actuator general purpose switch card with a custom backplate that housed the plugs.

Step	Instruction
1	Read Sample Temperature
2	Set Horizontal Configuration, Pause
3	Set Current, Pause then Read Voltage
4	Set Vertical Configuration, Pause
5	Set Current, Pause then Read Voltage

Table 2.1.: Basic program steps for a resistivity measurement. Setting configuration occurs at the data switch unit

2.3.4. Computer Data Acquisition

The data from the instruments is read by the computer using IEEE-488 (also known as GPIB) communication. The details of the communication are discussed in Appendix B. Measurements are taken when both cooling and warming, however only the warm up measurements are used for reasons discussed in section 2.2 on noise. The rate at which data is read is limited by the speed of the instruments. The HP 34420A nano volt meter has a built in function which integrates the measurement over a certain number of power supply cycles [22]. At 10 cycles (which was used for all measurements taken) a response time of ~ 0.5 seconds is given. In order to assure that the relays in the HP 34903A 20 channel actuator general purpose switch card were at rest[7] the measurement loop was paused for 0.5s after each configuration change in the unit. The measurement loop measures the resistivity in the basic steps outlined in table 2.1.

More time delay is introduced than shown by taking an average of several measurements for each configuration and due to the fact that this cycle is repeated for the second sample at position C. On average, for a single sample measurement it takes ~ 6 seconds for a single van der Pauw measurement to be taken. As discussed before, this time is

---

[7]Relays or switches tend to bounce when switched over, thus causing noise in the signal.

small compared to the thermal change in that time frame so noise is low, which also implies that the temperatures are approximately equal to each other when measuring each van der Pauw configuration. An averaging function is included in the program which averages the values over whatever temperature range is specified. Since there are many different instruments and connections, the program was made to include diagnostic tools to identify sources of troubles. Details of the program interface are included in Appendix C.

3. Theory

Before discussing the theories describing CDW and SC materials, a brief review of magnetism is necessary to understand certain aspects of their properties. Remember that the total magnetic dipole moment is defined as $\vec{m} = I\vec{a}$ where I is the current and $\vec{a}$ is the vector area [20]. A material may exhibit a magnetic field of its own without electrical current when there are tiny dipole sources through out the material. If $\vec{m}$ is the sum of all these magnetic dipoles throughout the material, we define magnetization as

$$\vec{M} = \frac{\vec{m}}{X}$$

Where X is a volume, mass or moles. For convenience, we will use the same units as the magnetic measurement system uses (see chapter on magnetic properties). Magnetization is measured in $\frac{\text{emu}}{\text{g}}$ where

$$1\text{emu} = 10^{-3}\text{A} \cdot \text{m}^2$$

The auxiliary field is measured in Oersted (Oe).

$$1\text{Oe} = \frac{1000}{4\pi}\frac{\text{A}}{\text{m}}$$

The total magnetic field in space is the sum of the auxiliary field, H (fields caused by a current), and the magnetization by $\vec{B} = \mu_o(\vec{H} + \vec{M})$. When the magnetization is a linear response in the auxiliary field we have $\vec{M} = \chi\vec{H}$ where χ is the magnetic susceptibility. Diamagnetism arises from orbital motion of the electrons and is present in all materials, and in general is very weak. Diamagnetism has a field that opposes the H field and therefore has negative susceptibility. Paramagnetism arises from the spin of the electrons attempting to align to the H field, and can only do so when there are unpaired electrons and is related to the density of states [21].

3.1. Superconductivity

Superconductivity is a state of matter for which the material has perfect conductivity and exhibits perfect diamagnetism. The original phenomenological explanation of zero resistance and the Meissner effect by the London brothers [23] was expanded by Pippard to the nonlocal generalized case[24]. Ginzburg and Landau in 1950 introduced the theory of superconductivity based on characterizing the superconducting electrons by a pseudo-wavefunction order parameter [25]. With this, spatial variations of the density of superconducting electrons could be calculated. Finally, the microscopic theory of superconductivity was put forth by Bardeen, Cooper, and Schrieffer in 1957 [1]. BCS theory predicted the isotope effect[1] and predicted that electron pairs (mediated by phonons) were responsible for superconductivity [1]. London showed[23] by taking the relaxation

---

[1]The isotope effect is the change in the SC transition temperature based on the mass of the isotope of superconducting material $T_c \propto M^{-\alpha}$. [26]

time to be infinite in the Drude model of conductivity that:

$$\vec{E} = \frac{\partial}{\partial t}(\Lambda \vec{J_s}) \tag{3.1}$$

where Λ is defined as

$$\Lambda = \frac{4\pi\lambda^2}{c^2} = \frac{m}{n_s e^2} \tag{3.2}$$

Here λ is called the London penetration depth, n_s is the density of superconducting electrons, e is the charge of the carrier, and m is the mass of the charge carrier. Equation 3.1 shows that for steady current, the electric field is zero. This is what we expect for superconductivity. In the same paper London showed

$$\vec{H} = -c\nabla \times (\Lambda \vec{J_s}) \tag{3.3}$$

If we substitute 3.1 into 3.3 we obtain

$$\nabla^2 \vec{H} = \frac{\vec{H}}{\lambda^2} \tag{3.4}$$

A particular solution to 3.4 is for an infinite flat slab superconductor in the YZ plane, where the superconductor exists everywhere $x > 0$, and a magnetic field strength of $\vec{H_o}$ exists everywhere outside the sample. The magnetic field inside the superconductor is then given [27] as

$$\vec{H}(x) = \vec{H_o}e^{\frac{-x}{\lambda}}$$

which makes it clear why λ is described as the penetration depth, since it describes the

penetration of a magnetic field into the superconductor. An important result follows for a flat slab of thickness d; it can be shown that [25] when $d \gg \lambda$ the susceptibility becomes:

$$M = -\frac{H_o}{4\pi}. \tag{3.5}$$

This perfect diamagnetism in superconductors is called the Meissner effect. The Meissner effect means that there is no magnetic field in the material which is implied by London's equations. The transition of the magnetization is sudden when entering the superconducting state. There is however a critical field at which superconductivity is lost [25] and which is approximated by $H_c(T) \approx Hc(0)[1 - (T/T_c)^2]$ where T_c is the critical temperature. Abrikosov investigated a different limit of Ginzburg Landau theory[2] and predicted that a mixed state might appear where the superconducting bulk would contain an array of flux tubes with superconducting vortices around them and cause a continuous transition in the magnetization instead [25]. This is called a type II superconductor, and the susceptibility is perfectly diamagnetic until it enters this mixed state at a critical field called H_{c_1}. It remains in the mixed state until a second critical field called H_{c_2}, above which it reverts to the normal state.

BCS Theory predicts that superconductivity is created by Cooper pairs: pairs of weakly attractive electrons mediated by phonons. BCS predicts the temperature dependent gap energy $\Delta(T)$ which is the energy to break a Cooper pair [1]. The temperature dependent gap function is shown in Figure 3.1.

---

[2]He investigated what would happen if the Ginzburg Landau parameter κ were large instead of small [25].
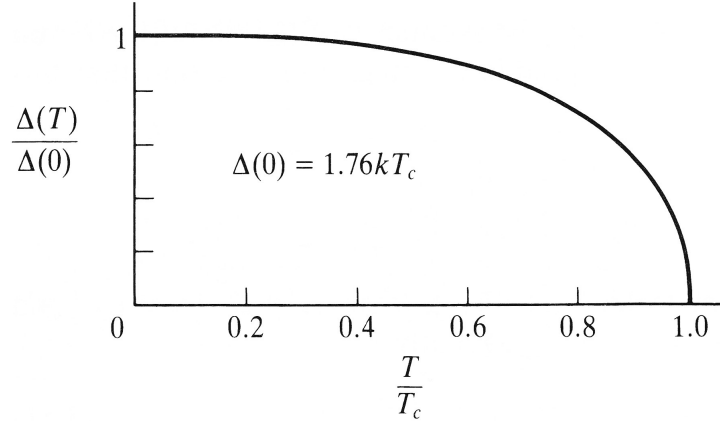
Figure 3.1.: Temperature dependence of the gap function. Reproduced from [25]

The energy of the zero temperature gap in BCS theory can be determined by the equation [28]

$$2\Delta(0) = 3.52k_BT_c \quad (3.6)$$

where k_B is the Boltzmann constant. The principle which the magnetic field breaks the pair (or sufficiently high current to generate a field to break the pairs) is when the landau splitting causes high enough energy to reach the gap energy (orbital vortex pair breaking) [29] or Zeeman splitting when the field is strong enough to split the energies sufficiently to exceed the gap energy (pauli pair breaking) [30][31]. So when measuring the SC transition temperature, it is important to use low fields and currents to prevent the Cooper pairs from breaking. The Meissner effect is utilized to find the superconducting transition temperature by susceptibility measurements.

3.2. Charge Density Waves

The concept of the charge density wave (CDW) was first theorized by Rudolf Peierls in 1930 [2]. A CDW is a periodic distortion of a quasi-one dimensional lattice producing a static wave distortion in the charge density along the lattice [3]. The mechanism that produces this distortion is an electron-hole condensate similar to the electron-electron Cooper pair of BCS theory. Coincidentally, the Ginzburg Landau theory in the long wavelength limit can be used to describe CDW [3]. One way to show how CDW comes about is to consider the Lindhard theory of screening in one dimension. It arises by considering a Schrödinger equation with a potential due to the lattice atoms and other electrons with charge screening in a free electron gas [32]. In the case that the screening charge density is linear in the potential, the dielectric constant becomes (Lindhard response function [3]):

$$\chi(\vec{q}) = \int \frac{d\vec{k}}{(2\pi)^d} \frac{f_k - f_{k+q}}{E_k - E_{k+q}} \tag{3.7}$$

where f_k is the fermi function at wavevector k, and χ is the dielectric susceptibility. If this is integrated for three or two dimensional fermi surfaces of a free electron gas energy

$$E_k = \frac{\hbar^2 k^2}{2m_e}$$

where m_e is the free electron mass, the result isn't very interesting. However, integration in one dimension around the Fermi energy[3] leads to a divergence around $q = 2k_f$ [3]. The three situations are depicted in Figure 3.2:

---

[3]linearized near the Fermi energy as $E_k - E_F = \hbar v_f(k - k_F)$.
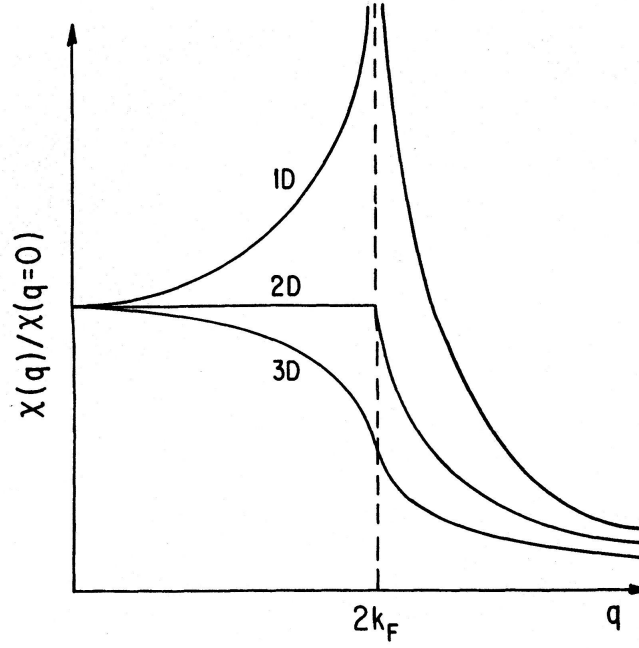
Figure 3.2.: Wavevector dependent Lindhard response function for a one-, two- and three-dimensional free electron gas at zero temperature. Reproduced from [3].

This shows that there is a lowering of energy for an electron at $-k_F$ and hole at $+k_F$. This electron-hole pair produces a gap (thus reducing the energy) in the electronic dispersion relation near $\pm k_f$. This new state causes a static periodic distortion of the lattice and charge as shown in Figure 3.3

In 1959 Kohn proposed that CDW would cause a discontinuity in the phonon dispersion where a notch is formed around $2k_f$ [33]. This is shown in Figure 3.4.

In CDW there is a gap function that describes the energy needed to destroy the pairs, analogous to the BCS gap function. This gap function forms suddenly producing a second order phase transition. In superconductivity, the Cooper pair has a net charge
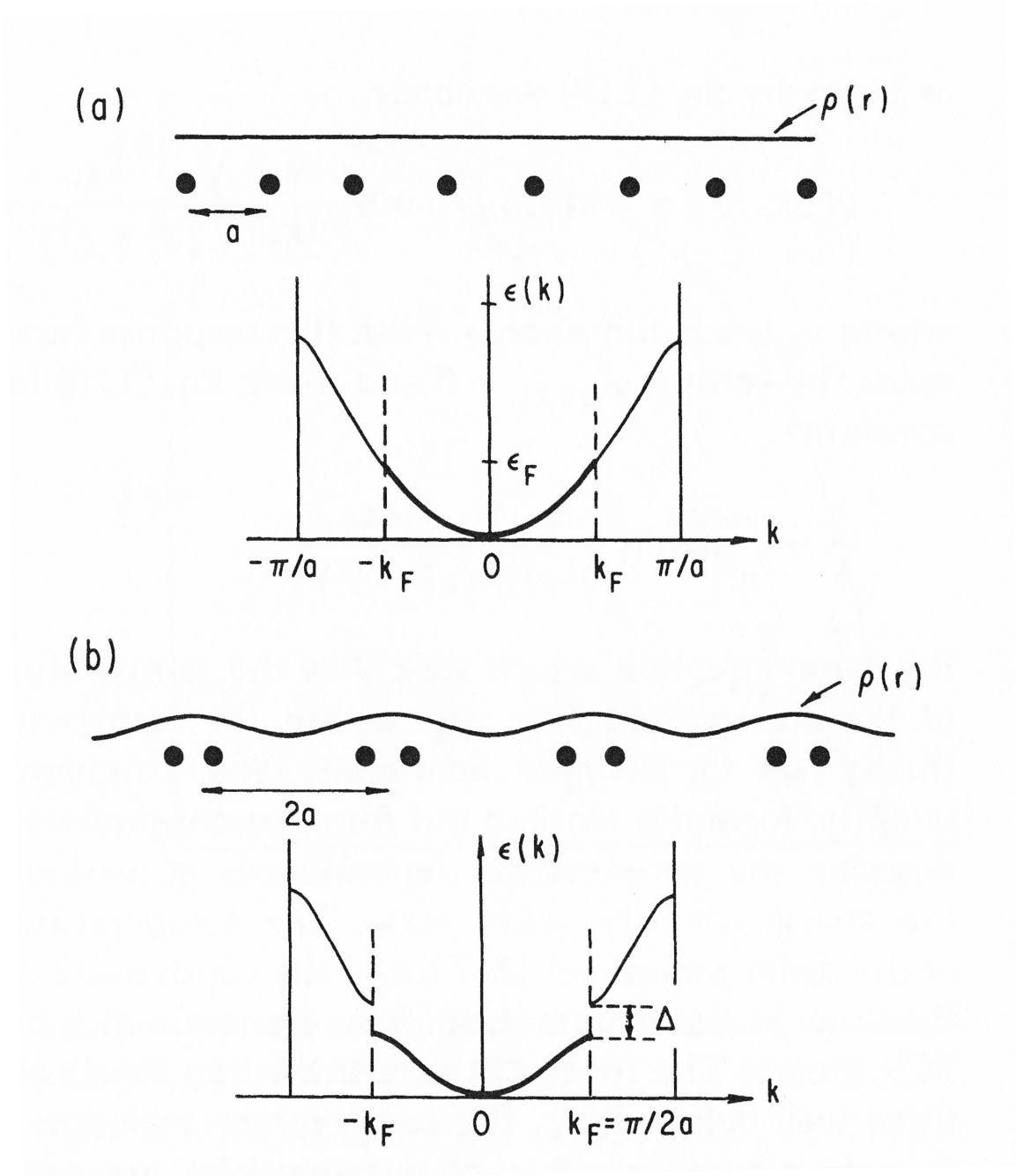
Figure 3.3.: a) The charge density on a one-dimensional lattice, and below it, the dispersion relation of a free electron model of a metal. b) In the CDW state the lattice and charge density has a static periodic distortion. Below, it shows that a gap of size Δ opens in the dispersion relation. Reproduced from [3].
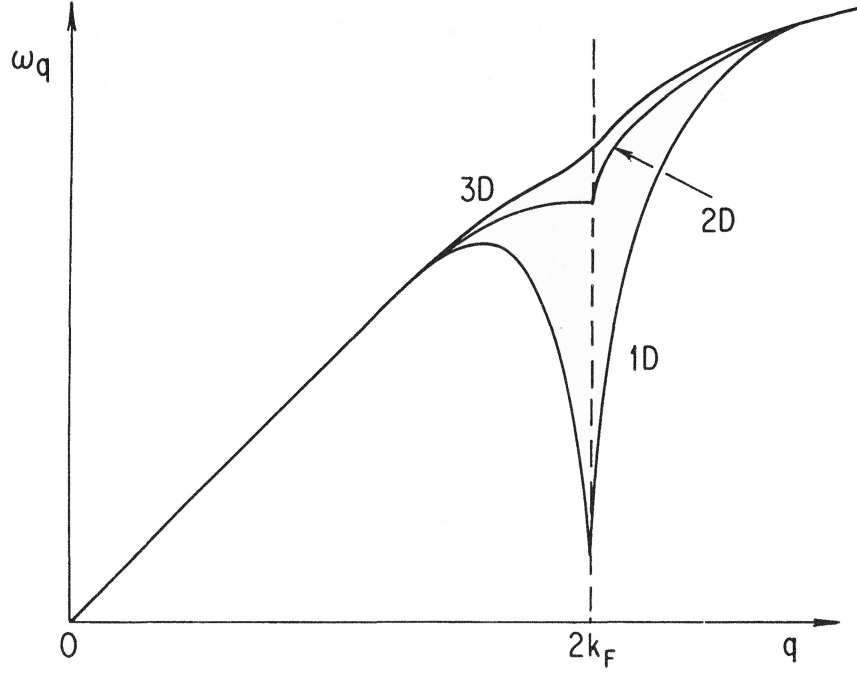
Figure 3.4.: Acoustic phonon dispersion relation of one-, two-, and three-dimensional

metals. Reproduced from [3].

thus contributes to conduction. However, it is important to note that the electron-hole

pair bosonic quasi-particle (amplitudon) is charge neutral and has an interaction with

impurities and lattice imperfections, which causes it not to contribute to DC conduction.

The introduction of the gap however causes resistivity to increase. The onset of this

defines the CDW transition [3].

4. Magnetic Properties of $Cu_x TiSe_2$

Several samples of $Cu_x TiSe_2$ were selected from a crystal growth carried out by Artorix de la Cruz de Ona at Brock University. The dopings of the samples were not known. In order to test the resistivity system that was constructed, a set of DC magnetic susceptibility measurements were done on these samples to characterize their superconducting transition temperatures. These measurements were conducted in a Quantum Design Inc. Magnetic Property Measurement System (MPMS). The MPMS measures the susceptibility by applying a field, then physically transporting the sample through a set of counter-wound coils, which pick up the change in induction measured with a SQUID. The magnetic susceptibility is then calculated based on the EMF measured and corrected by a correlation table [34]. The temperature range of the MPMS is 1.9K - 400K [34]. The sample was placed in a plastic capsule with some vacuum grease to prevent the sample from moving while being transported in the MPMS and oriented such that the a-b plane was parallel to the $\vec{H}$ field. Measurements were compared to results from E. Moroson et al. [5] to determine the doping concentration x. A temperature dependent measurement was conducted at 0.5T field strength from 300 K to 1.8 K on sample 1,

shown in Figure 4.1.

In Figure 4.1 a) it can be seen that at high temperature the susceptibility is positive and then, as temperature decreases, drops at a certain temperature. This temperature is the transition temperature into the CDW state which causes the susceptibility to decrease once the gap in the dispersion relation is formed. This is because the electronic density of states drops, and the contribution from Pauli paramagnetism is reduced, and the core diamagnetism begins to dominate [5]. The magnetization then rises with Curie-Weiss like behavior as temperature is further lowered until it drops to pure diamagnetism below the SC transition temperature. Figure 4.1 b) shows the measurement on Sample 1. There appears to be a shift in the data to negative susceptibilities. This may have been a diamagnetic shift due to an improper correlation table loaded in the MPMS to account for the grease. However, the importance for determining the doping is in the temperature dependent features and the absolute offset is not important. The data is quite noisy but it can be approximated that the CDW transition temperature is around 120 K. Comparing Figure 4.1a) to 4.1 b) we can estimate the doping to be between x=0.03 and x=0.04.

In small fields we can observe the SC transition at low temperatures to characterize the doping of the sample. E. Morosan et. al. measured [5] the critical fields for polycrystalline Cu$_{0.08}$TiSe$_2$ at 3.5 K to be $H_{c_1} \approx 18$ Oe and $H_{c_2} \approx 3000$ Oe. The zero temperature values are $H_{c_1} \approx 0.12$ T and $H_{c_2} \approx 1.33$ T. In Sample 1, a field of 10 Oe was applied parallel to the a-b plane to observe the SC transition. The results (shown in Figure 4.2) show a SC transition temperature of about 3.6K. This suggests by comparison to data
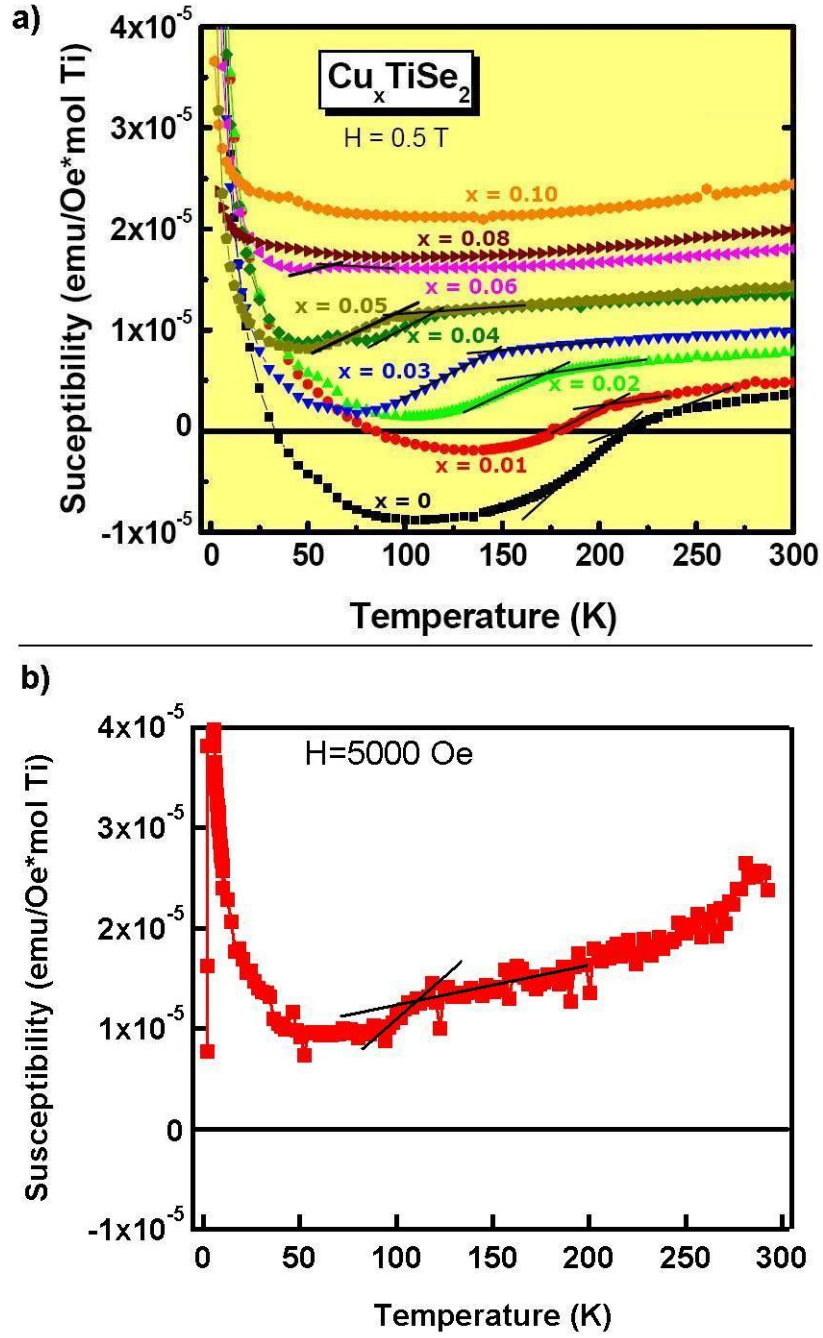
Figure 4.1.: Temperature dependence of the magnetic susceptibility in $Cu_x TiSe_2$ for a field strength of 0.5T. a) Results from E. Moroson et al. [5]. b) Results from Sample 1. Absolute value was shifted down due to diamagnetic contribution from the capsule and grease used to hold the sample. Shows the CDW transition temperature at ≈ 120 K

from Figure 4.2 a) that the doping is between x=0.06 and x=0.1.

A second sample (Sample 2) was also characterized for the SC transition with the field of 10 Oe parallel to the a-b plane of the sample. The results are shown in Figure 4.3. The SC transition temperature appears at about 2.5K which would suggest a doping between x=0.055 and x=0.06.

The comparison of the results for the SC transition from E. Morosan et al. [5] to measured data on Samples 1 and 2 is not ideal to characterize the doping. The SC transition curves in Figures 4.2 b) and 4.3 b) do not seem to have the same slope as the data of E. Morosan et al. [5]. This may be the result of having a range of doping in a single crystal due to different doping concentrations in different regions of the crystal causing a range of transition temperatures. E. Morosan et al. [5] performed measurements on polycrystalline samples, which may behave differently than a single crystal since all crystal orientations are taken into account with polycrystalline samples while Samples 1 and 2 were measured with the H field parallel to the a-b plane. Notice in Figures 4.2 a) and 4.3 a) that the transition temperature increases with doping from x=0.55 to x=0.08. However, above doping of x=0.08 there seems to be a turning point, which causes doping of x=0.10 to go to a lower SC transition temperature. It is not clear from this measurement whether the doping is above or below the peak SC transition temperature concentration. The result can however be compared to other measurement techniques to find the doping to look for consistency.
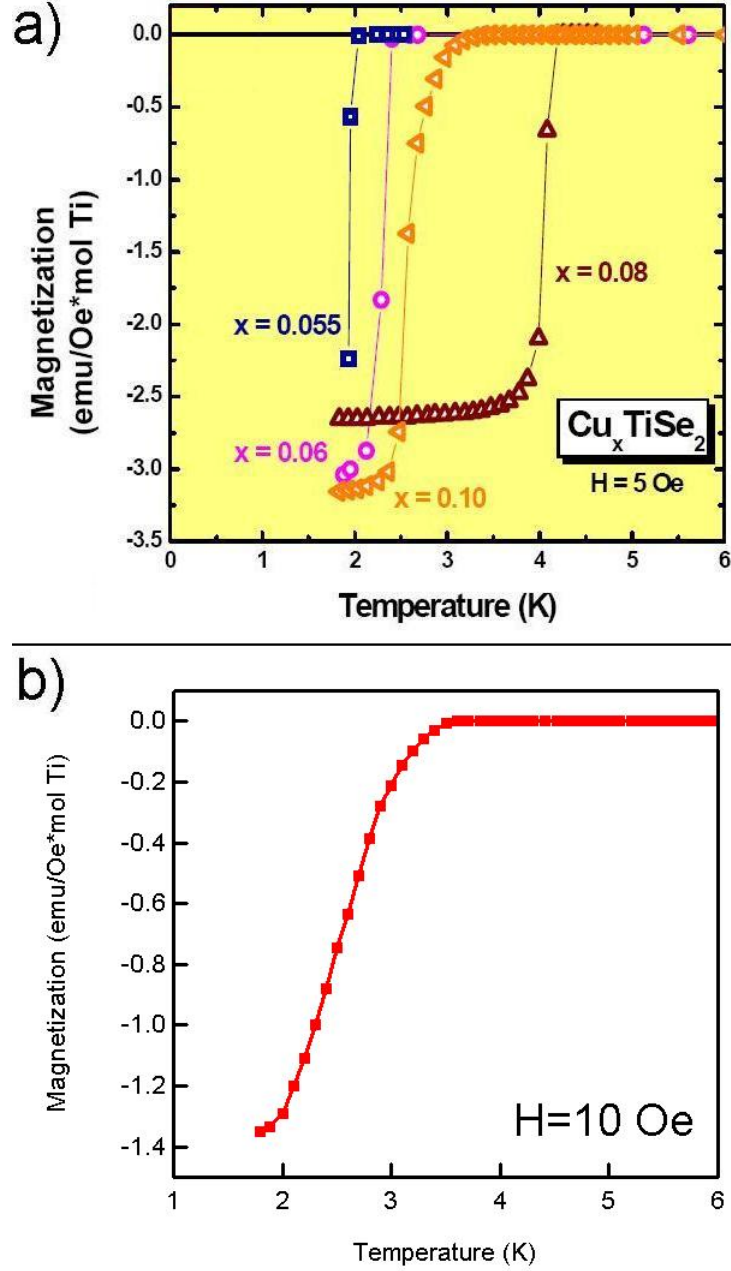
Figure 4.2.: Temperature dependence of the magnetic susceptibility in $Cu_x TiSe_2$ for low field strength around the SC transition. a) Polycrystalline data from E. Morosan et al. [5] at 5 Oe. b) Sample 1 (a single crystal) magnetization for a field strength of 10 Oe. SC is observed with an onset at ~ 3.6K.
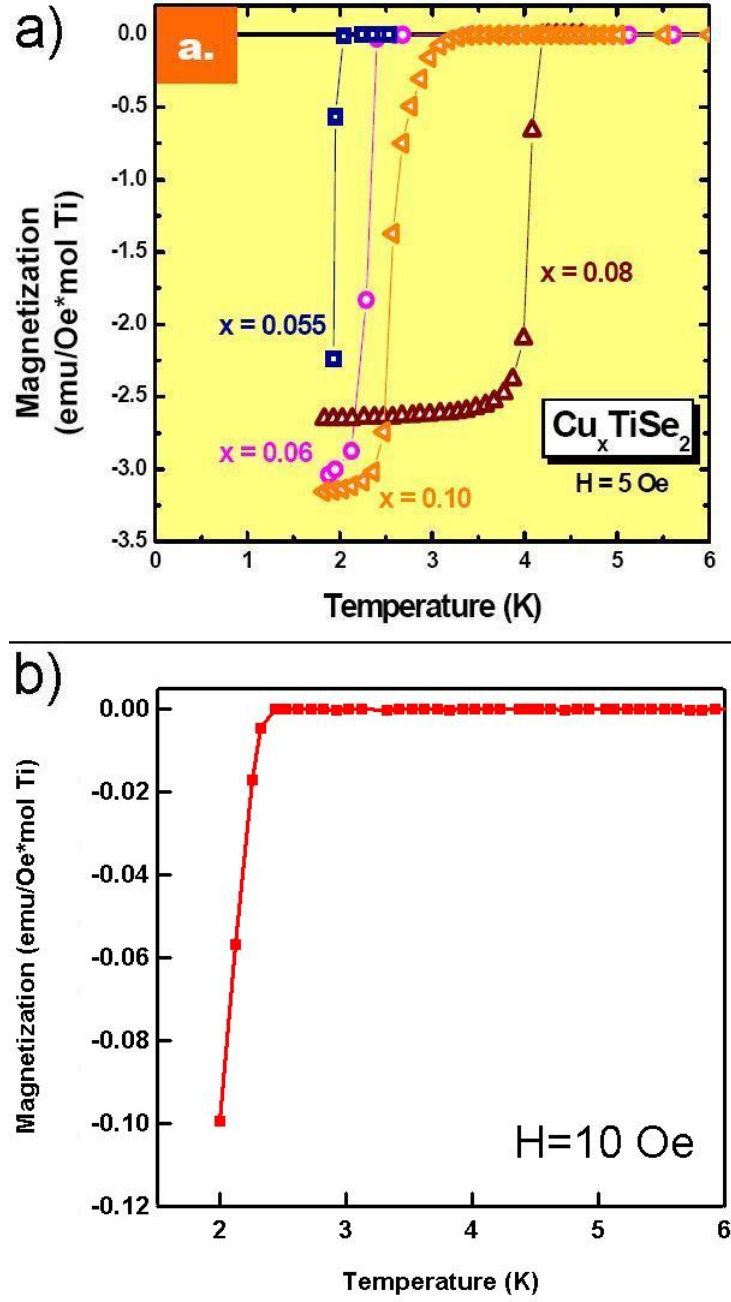
Figure 4.3.: Temperature dependence of the magnetic susceptibility in $Cu_x TiSe_2$ for low field strength around the SC transition. a) Polycrystalline data from E. Morosan et al. [5] at 5 Oe. b) Sample 2 (a single crystal) magnetization for a field strength of 10 Oe. SC observed with an onset at $\sim$ 2.5K.

5. DC Transport Properties of Cu$_x$TiSe$_2$

Resistivity measurements were conducted in the a-b plane on the same samples of Cu$_x$TiSe$_2$ (as in the magnetic properties chapter) using the resistivity measurement system constructed. The CDW transition temperature and SC transition temperature was extracted. Measurements show a broad maximum which agrees with other groups [8][5]. Low temperature measurements[1] did not have the slow rate[2] to obtain ideal low noise measurements due to unforeseen technical difficulties. Time constraints did not allow the measurements to be repeated. Typical contact resistance was between 3Ω and 12Ω. The results for Sample 1 are shown in Figure 5.1 b) with a power law forced fit to emphasize the CDW bump.

In Figure 5.1 a), the CDW state produces an increase in resistivity manifesting in a broad peak centered around 90 K. By comparison with the data shown in Figure 5.1 a), the doping of Sample 1 appears to be in the range of x=0.055 to about x=0.065.

---

[1]Temperatures utilizing the He^3 system on the cryostat.

[2]Rate of change of temperature with time.
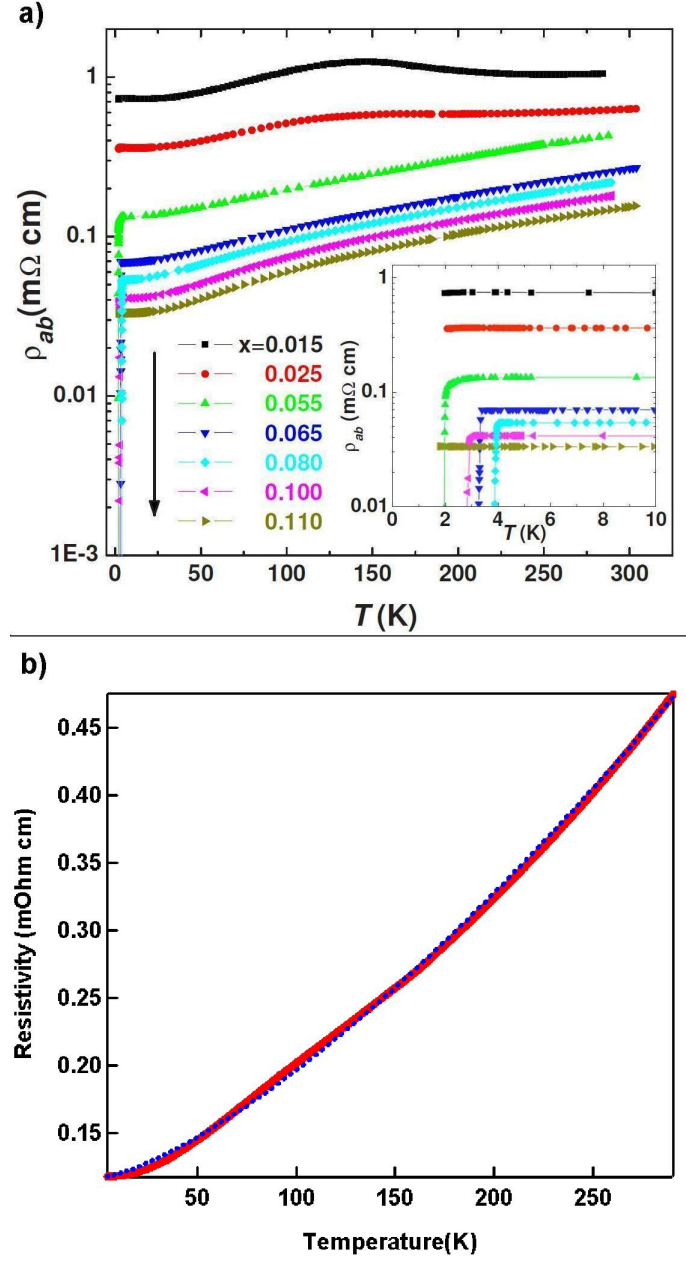
Figure 5.1.: Temperature dependence of the resistivity in Cu_xTiSe$_2$. a) Results for different dopings on single crystal samples in the a-b plane reproduced from [8]. b) Resistivity of Sample 1 measured in the new resistivity system. Shows a CDW transition temperature of $\approx$ 162K. The dotted line is a power law forced fit that emphasizes the CDW bump.

The beginning of the bump signifies the onset of the CDW state. However, the start of this bump is very hard to observe for a weak CDW state. Theory suggests that the onset of CDW must be quite sudden since the gap suddenly forms at the transition temperature. No function is known to fit to the resistivity data. A polynomial of infinite order theoretically would fit the curve exactly, but for lower orders the polynomial will fit the smooth parts of the resistivity data while the sudden increase introduced by the second order phase transition wouldn't be fitted sufficiently. If we call the polynomial fit to the resistivity data above the SC transition of nth order $\rho_{n^{th} \text{ order}}$, and the data $\rho_{\text{experiment}}$, then the base line fit is defined as:

$$\rho_{bl,n}(T) = \rho_{\text{experiment}}(T) - \rho_{n^{th} \text{ order}}(T) \tag{5.1}$$

The base line fit given by equation 5.1 can show the sudden spike that marks the CDW phase transition. Taking the second derivative of the data would also reveal the CDW transition temperature but the noise in the measurement prevented this method from clearly showing the feature in the second derivative (shown in Figure 5.2). Plots of the base line fits for 7-10th order are shown in Figure 5.3.

There is a clear common bump in all orders around 162K. Assuming that other bumps that are not common between the orders are just continuous (smooth) portions of the data that are not fitted properly, we can assume this is the sudden onset that we have been looking for, which is the transition temperature to the CDW state. However, this value doesn't appear to correspond to the value obtained by magnetic susceptibility. Discrepancy could be explained by the fact that E. Morosan et al. [5] used a different method of identifying the CDW transition temperature. Notice that the noise is quite
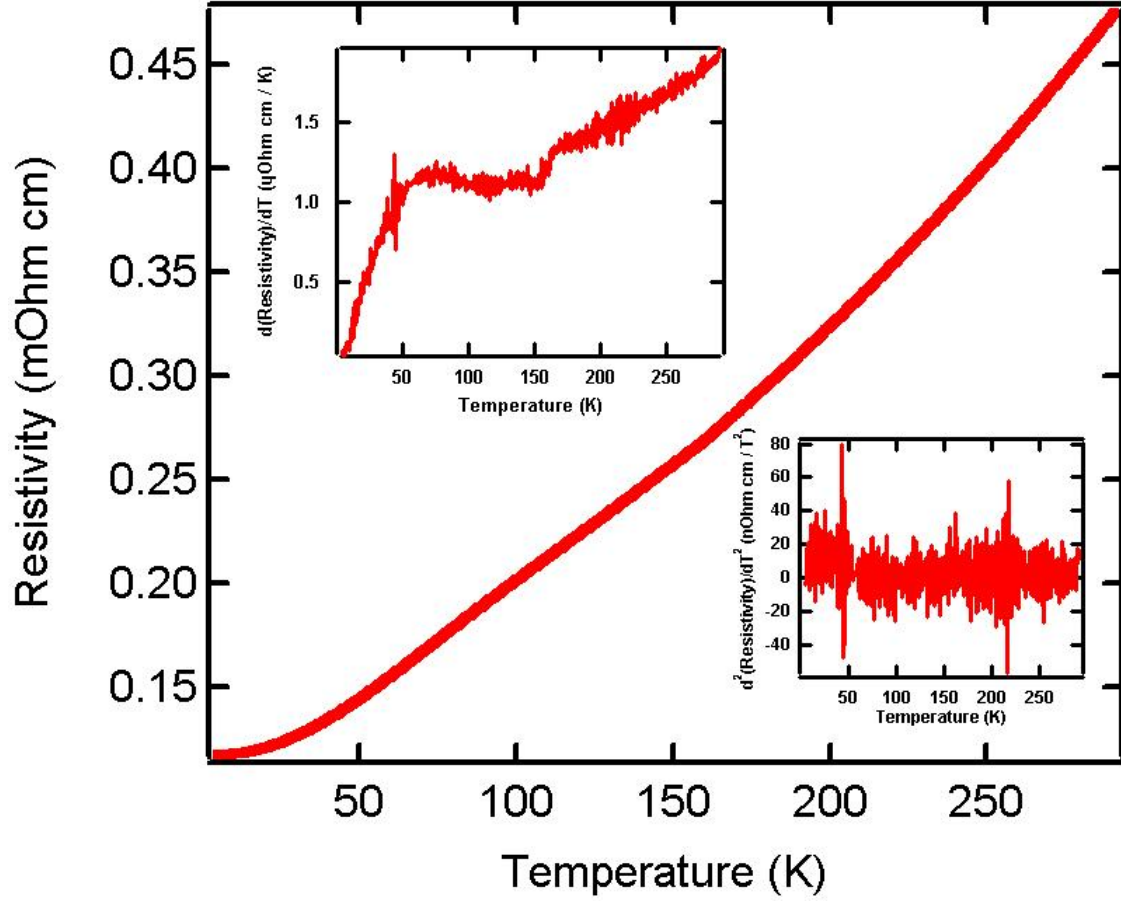
Figure 5.2.: Resistivity of Sample 1. The top left inset shows the first derivative of the data. The bottom right inset shows the second derivative of the data. The CDW feature is not visible beyond the first derivative.
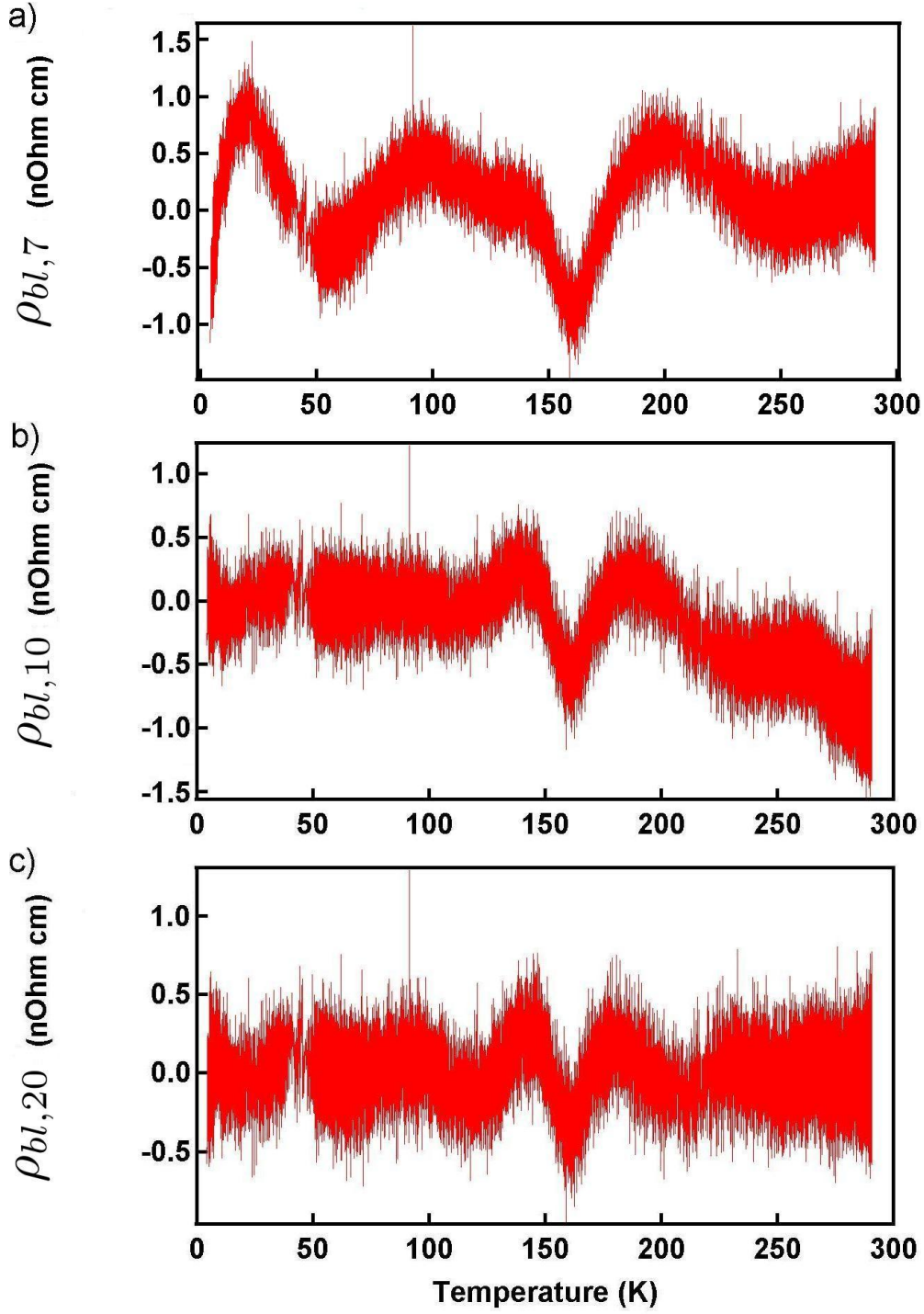
Figure 5.3.: Polynomial baseline fit on resistivity data for Sample 1. There is a clear common dip at 161K which could be the CDW transition. a) Seventh order. b) Tenth order. c) 20th order.

significant in the base line fit. V_{RMS} values in the new measurement system on this sample were around $4.5\,nV_{RMS}$. In the old system, a measurement was taken on the same sample, where the results didn't produce anything that could confidently be extrapolated for the CDW due to noise wash out (shown in Figure 5.4).
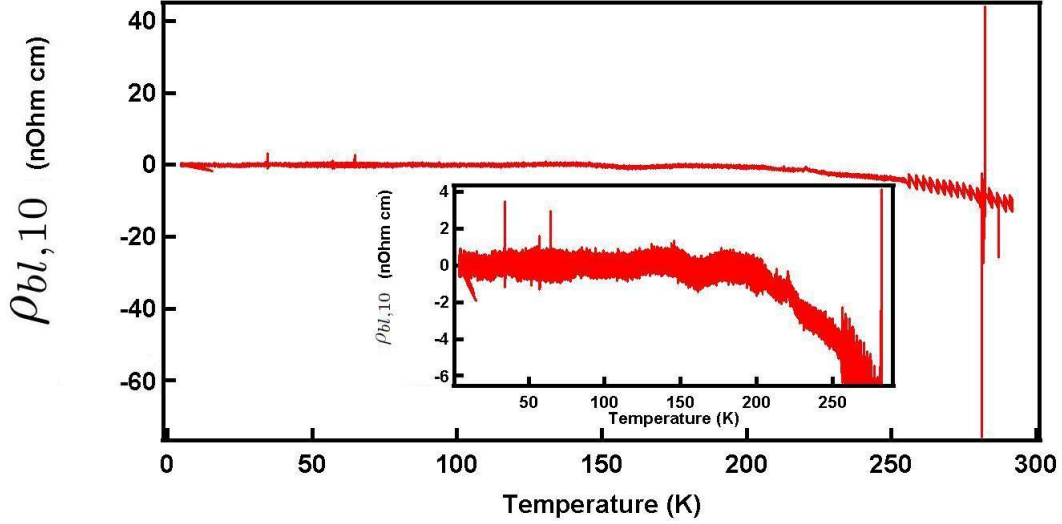
Figure 5.4.: Tenth order polynomial baseline fit on resistivity data measured on old resistivity system for Sample 1. Notice the peak to peak noise is magnitudes of order higher (up to $10^{1.5}$ higher). Note that the peak is still faintly visibly in the inset tenth order poloynomial base line fit at 161k, however other features on this graph could easily be mistaken for the same transition.

In Sample 2, the noise reduction of the new system can be dramatically observed. Sample 2 is an elongated sample with an aspect ratio of roughly 1:3, with the largest dimension being roughly 7mm. As discussed in section 2.2.1, noise on elongated samples can be quite high. Sample 2 was measured in the old system from 77 K-300 K, while in the new system it was measured between 4 K - 300 K. The results are shown in Figure

5.5.

When comparing the results of the new measurement in 5.5 b) to 5.1 a) we approximate the doping to be between x=0.025 and x=0.015. The CDW bump appears to be centered around 125 K. The CDW transition occurs at $\sim$ 166 K as determined by a polynomial baseline fit.
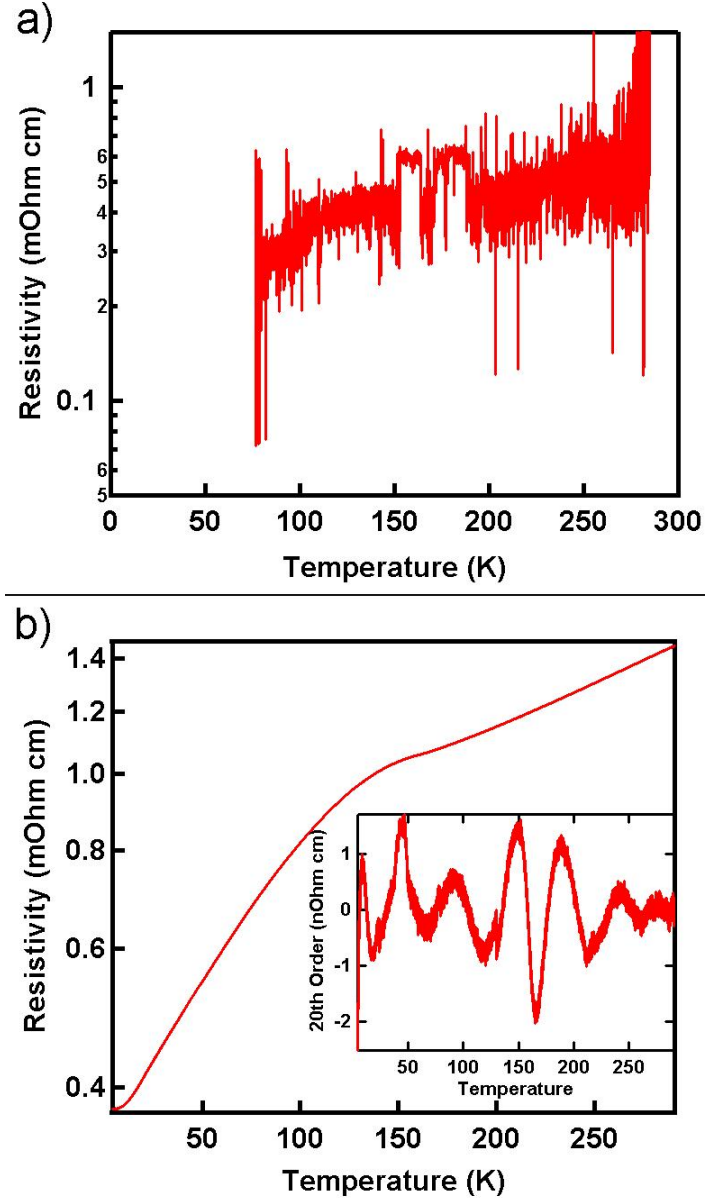
Figure 5.5.: Temperature dependence of resistivity in Sample 2, Cu$_x$TiSe$_2$ in the two different systems. a) Results in the old measurement system from liquid nitrogen temperatures. b) Results in the new resistivity measurement system from liquid He^4 temperatures. Inset shows a 20th order polynomial baseline fit showing a CDW transition of 166 K

6. Conclusions

A resistivity measurement system was constructed and interfaced in a user-friendly manner to perform low noise resistivity measurements. The noise on the voltage measurements was reduced from $\sim$15 nV$_{RMS}$ to $\sim$4.5 nV$_{RMS}$. This noise reduction was crucial for the determination of the CDW transition for low doped Cu$_x$TiSe$_2$ samples.

Sample 1 was determined to have a CDW transition at $\sim$162K by the resistivity measurement, and a transition temperature of 125K by the field dependent magnetization MPMS measurement (see Figure 6.1).

The determination of the CDW transition temperature by resistivity was done by a high order (8-20 order) polynomial base line fit, which revealed the discontinuity in the data and is assumed to be the CDW transition point. The determination of the transition temperature through the resistivity measurement in the old resistivity measurement system was not possible due to the noise washing out the features. The values for the CDW transition are not similar but it is noted that the magnetization data was being compared to polycrystalline samples. The SC transition temperature measurement showed a wide transition which may have been due to doping inhomogeneity. The
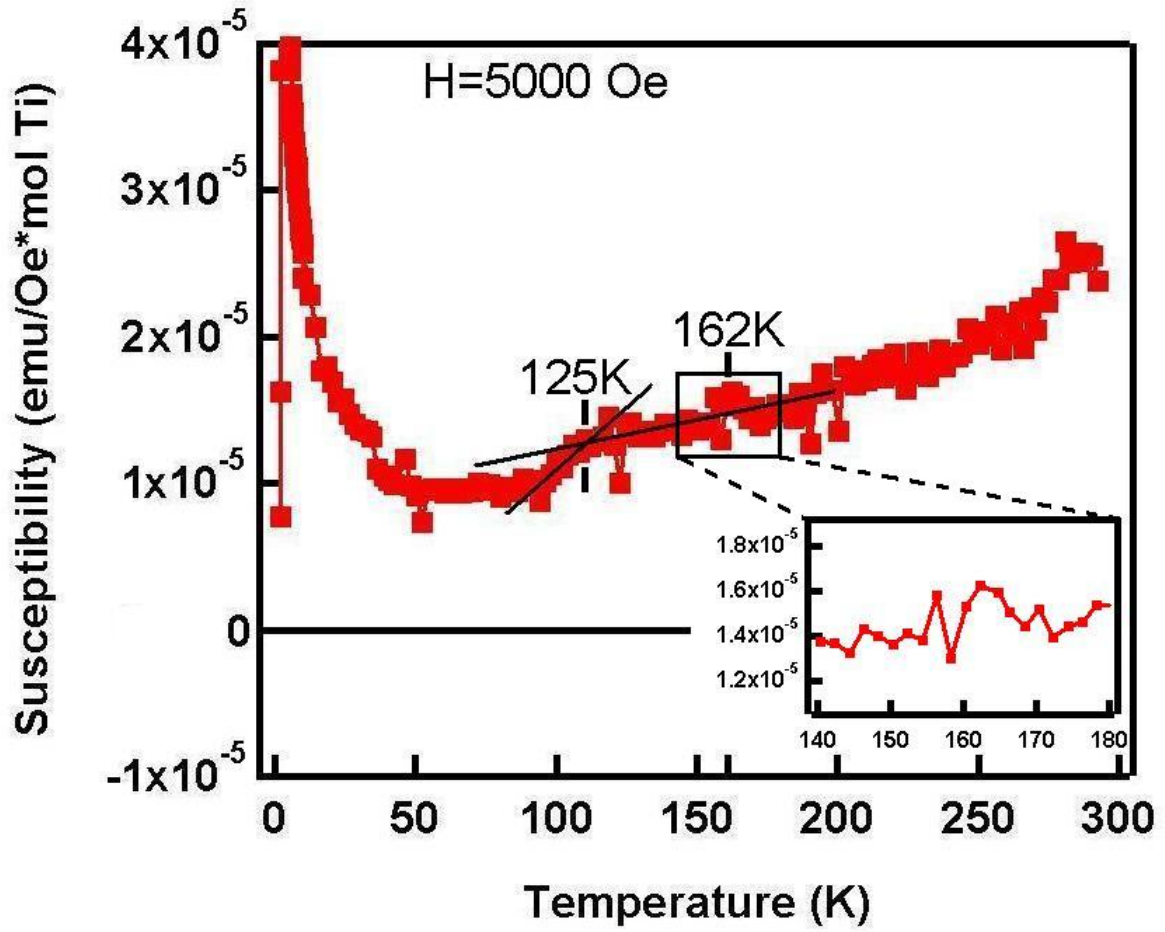
Figure 6.1.: Temperature dependence of the magnetic susceptibility in Cu_xTiSe_2 for a field strength of 0.5T for Sample 1. Absolute value was shifted down due to diamagnetic contribution from the capsule and grease used to hold the sample. Shows the CDW transition temperature at ≈ 120 K and identifies the CDW transition temperature as identified by the resistivity measurements at ≈ 162 K. There is a small feature around 162 K (see inset for expanded view) which might identify as the CDW transition temperature if the measurement was conducted with more resolution in that region.

base line fit method might have also skewed the results since the dip may not have corresponded to a discontinuity in the resistivity but may have been the result of measurement fluctuations or fluctuations in the polynomial fit. Other bumps in the base line fit may have corresponded to other CDW transitions due to regions of different doping in the sample. Comparing the estimations for the doping, Sample 1 was determined to be between x=0.055 to x=0.065 with resistivity, between x=0.06 and x=0.08 by the small field magnetization measurement detecting the SC transition, and between x=0.03 and x=0.05 for the high field magnetization measurement. Again, it appears that the high field magnetization measurement is not within the range for other measurements due to comparing single crystals to polycrystalline samples and doping inhomogeneity in the samples. The true range is thus assigned to be between x=0.06 and x=0.065 using results of the resistivity and SC transition measurements.

In Sample 2, the high resistivity data shows low doping at a doping parameter between x=0.025 and x=0.015, while the SC transition showed that the doping may be between x=0.055 and x=0.06. Resistivity measurements on Sample 2 showed high noise in the previous measurement system which was eliminated using the new measurement system. These doping concentrations do not agree with one another. It appears that the resistivity measurement shows that Sample 2 should have inhomogeneous doping since the phase diagram of $Cu_X TiSe_2$ showed that no SC transition exists for dopings below x=0.045 (see figure 1.1) while the resistivity data shows a higher slope and lower doping. This skewed result may have also been a result of not measuring exactly on the a-b plane. Cleaving only gave a rough estimate of the crystal orientation, X-ray diffraction

Sample 1	High Field Susceptibility	Low Field Susceptibility	Resistivity
T_{CDW}	125K		162K
T_C		3.6K	
Doping Factor x	0.03 - 0.04	0.06 - 0.10	0.055 - 0.065

Table 6.1.: Results for Sample 1.

Sample 2	Low Field Susceptibility	Resistivity
T_{CDW}		166K
T_C	2.5K	
Doping Factor x	0.055 - 0.06	0.015 - 0.025

Table 6.2.: Results for Sample 2.

must be used to determine the true orientation. The SC transition measurement may also have given an incorrect value for the doping since the transition temperature does not change linearly with doping [5].

These measurements demonstrate that the reduction in noise of the new resistivity measurement system has made the determination of crucial material properties possible, which would have been either inaccurate or impossible using the previous resistivity measurement system.

7. Future Research Directions

There are two directions for the future of this research. In the instrumentation, introduction of a source of uniform magnetic field into the cryostat would make possible the measurements of the Hall effect using van der Pauw method. This measurement would be able to detect the CDW transition that occurs in $Cu_X TiSe_2$ since it can measure the change in the dominant carrier type [8]. An additional 32 pin plug could be installed on the cryostat to make possible more sample measurements simultaneously to conserve liquid helium. It takes roughly 25L of liquid helium to produce one cool down to low temperatures. The old resistivity measurement system would cost roughly of \$500 per measurement. With another 32 pin plug, up to eight samples [1] could be measured simultaneously making a measurement on a single sample cost only \$60. MPMS calibration measurements should be done on the thermal grease to check if its calibration was distorted over time or if the grease changed.

To detect the transition temperature more accurately, X-ray diffraction measurements for a single crystal to determine precisely its orientation would improve the results of

---

[1]Limited to the space available on the sample and bolometer stages

any measurement. CDW is a quasi-two dimensional phenomena in $Cu_X TiSe_2$, therefore any measurement of values which are directionally dependent would be affected. Optical measurements on $Cu_X TiSe_2$ could also be performed in the same cryostat. Optical conductivity shows two peaks in the frequency spectrum, one for a resonance that follows a Drude-Lorentz model, and another peak that characterizes the single particle excitations at the energy of the gap [35][3]. The CDW transition temperature would be easier to detect by checking for their characteristic peaks.

7.1. Magneto-optical

During this thesis work, an interesting phenomena presented itself: R.C. Morris discovered [36] that in the superconducting material $NbSe_2$ the 2D CDW state can be suppressed by applying a field parallel to the c-direction while at the same time SC is enhanced. New evidence from D.W. Shen et. al. [6] shows that 2D CDW materials may have multiple 1D CDW vectors. It would be interesting to investigate the pair breaking mechanism for the electron-hole pair of the CDW by trying to suppress one of the CDW vectors while having the rest unaffected. This could be achieved by applying a magnetic field parallel to the a-b plane if the pair breaking mechanism was the orbital pair breaking. Polarized reflectance spectroscopy measurements would reveal which angle of polarized light would produce the typical CDW optical conductivity peaks and therefore would probe for individual CDW vector suppression. Instrumentation for this kind of measurement is being constructed as part of Jason Iwachow's Ph.D. thesis. The

instrument under design is an adapter for the cryostat such that high field neodymium magnets are held in a rotating device in the cold chamber such that it will rotate in the a-b plane of the sample while reflectance measurements can be taken parallel to the c direction. The rotator has been constructed and is shown in Figure 7.1.

Figure 7.1.: Photograph of the part of the magneto-optic measurement device that will rotate two large neodymium magnets around the sample inside the cryostat. Designed by Jason Iwachow.

A. Pressure Induced Noise

It was observed that cool down data in the resistivity system yielded characteristic jumps when changing the cooling fluid. An example of what occurs is shown for resistivity taken in the previous resistivity measurement system with Sample 1 in Figure A.1. The jumps occur at 300 K when liquid N_2 was filled and at $\sim$77 K when liquid He^4 began to transfer into the vessel.

The amplitudes were too large to be taken into account by simple thermoelectric effects. Further investigation to determine the cause has found that this is a pressure dependent effect that causes the voltage to change. Using the new resistivity system, a steel disk with spot welded contacts was utilized as the sample[1] to locate the source of noise. Base noise levels were on the order of 4.5 nV$_{RMS}$. At room temperature the voltage across two contacts was recorded as a function of time. The vacuum pump connected to the cryostat cavity was turned on causing a large voltage shift (Figure A.2).

This can be safely assumed to be independent of the wiring and instruments from the

---

[1]Spot welded contacts were utilized to prevent contact breaking on the sample
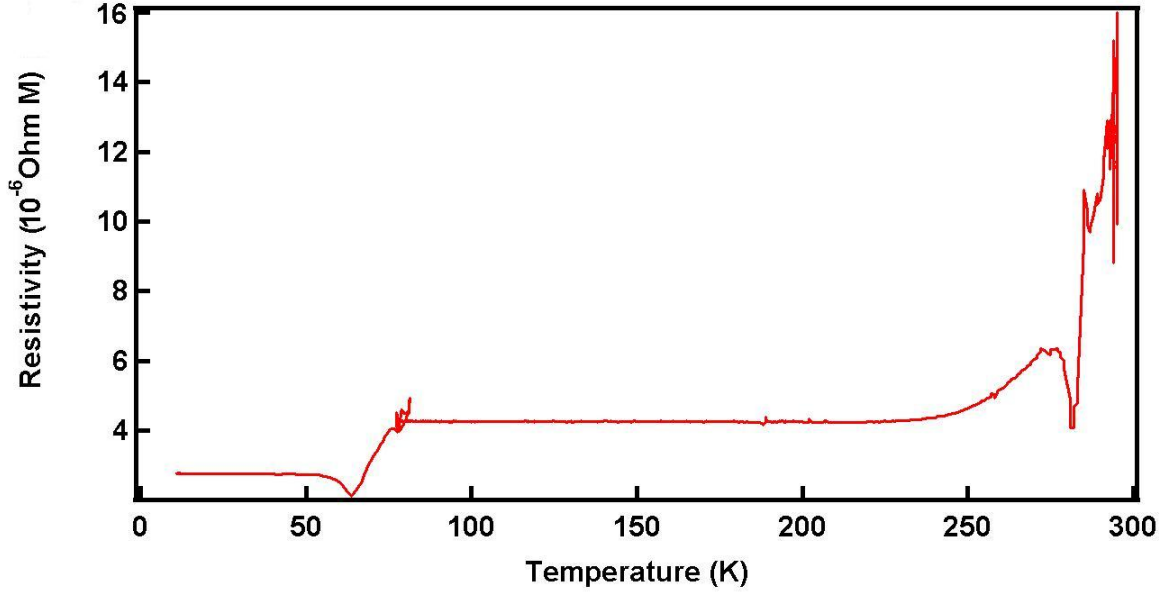
Figure A.1.: Cool down data in the previous resistivity measurement system using the same HDL-10 He^3 cryostat on Sample 1. Notice the jumps at 300 K when liquid N_2 is filled and $\sim$77 K when liquid He^4 begins to transfer into the main vessel.

outside to the 32 pin plug on the cryostat. This effect was not a property of the material being measured. To further determine the source of this noise, the sample holder was removed, the IC SIP resistivity measurement plugs (see Figure 2.4) voltage pins were shorted, and pressure dependent measurements were taken reading the shorted plugs. Voltage spikes were observed when pressure was increased or decreased (Figure A.3).

A possible explanation for this phenomenon is that the current carrying wires are in the same bundle with the voltage signal wires inside the cryostat. Pressure or temperature will cause a slight expansion or compression of these wires relative to each other which could induce an electromotive force (EMF). This agrees with the spikes in Figure A.3
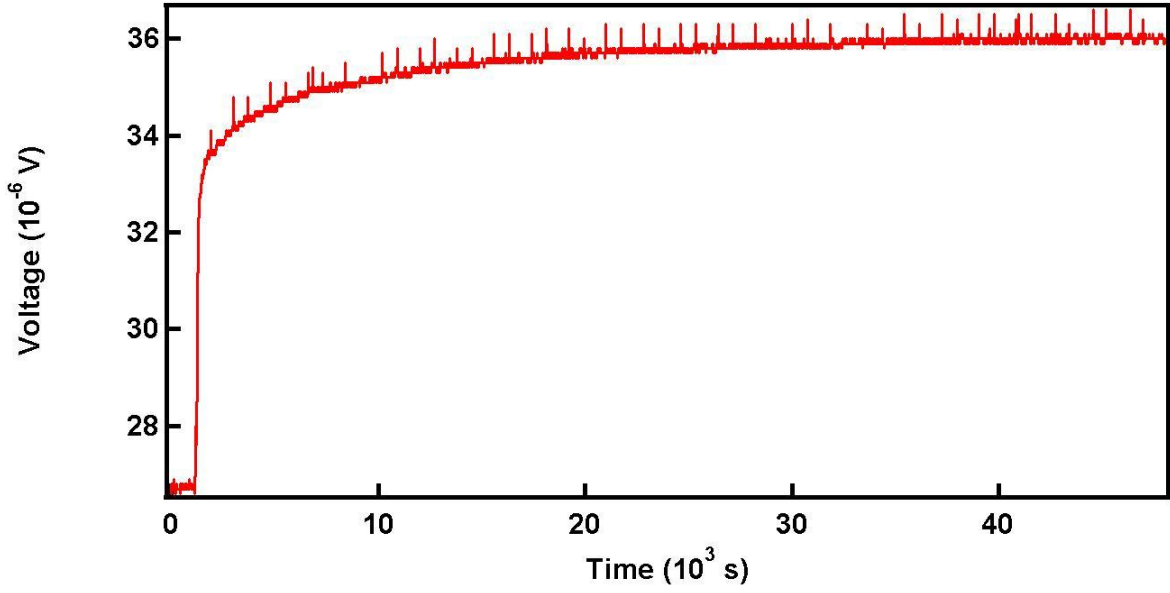
59

Figure A.2.: Room temperature ($\sim$295 K) voltage measurement on a steel disk in the current resistivity measurement system. At 1150s into the measurement the vacuum pump was turned on.

since the EMF would be opposite in sign for expansion/compression as well as for the fact that the spike for removing vacuum is larger than in evacuating since the pressure change is faster when removing the vacuum line to vent to atmospheric pressure. The voltage on the steel disk (Figure A.2) doesn't drop back to the value before evacuating as in the shorted case possibly due to capacitive effects in the instrument setup. This source of noise can be largely eliminated by evacuating first and maintaining low pressure while measuring as well as utilizing the quasi-static temperature measurement process described in section 2.2.4 whereby any slow variation of the voltage will be canceled out.
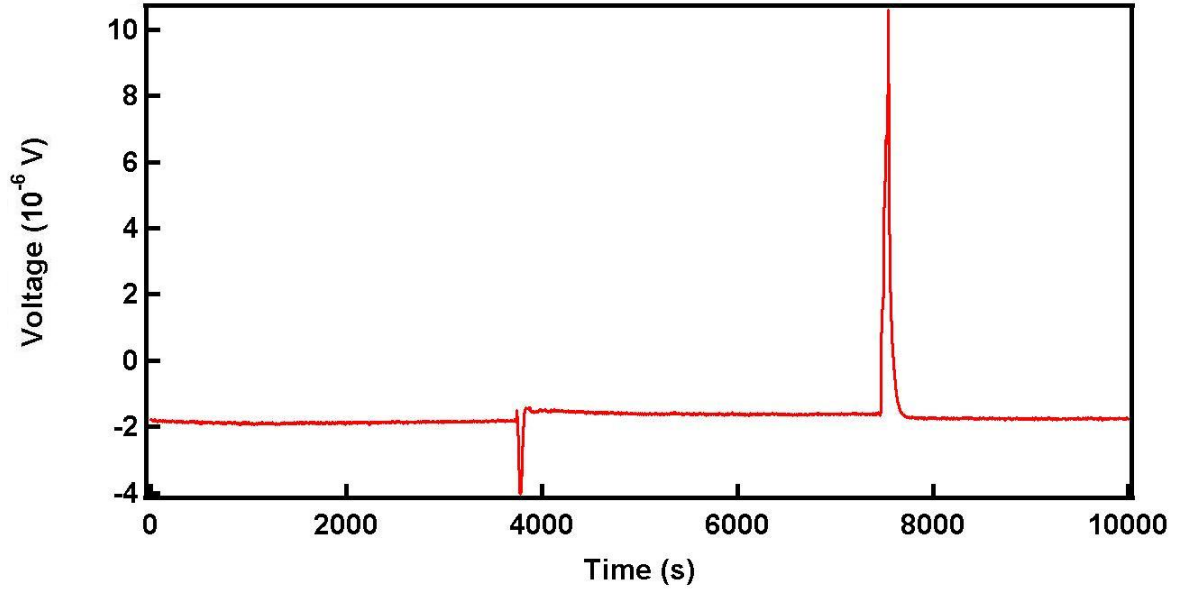
Figure A.3.: Room temperature ($\sim$295 K) voltage measurement for a shorted contact on the sample plug inside the cryostat. Vacuum was introduced at 3740s, where a voltage spike is introduced. Atmospheric pressure was observed at 7460s, which shows a voltage spike of opposite direction.

B. GPIB Communication

General Purpose Interface Bus (GPIB) is a common abbreviation for National Instruments standard IEEE-488. Most scientific measurement equipment uses IEEE-488 or RS-232 standards. The advantages of GPIB are that it is common, rugged, and can connect up to 15 instruments to a single card in a daisy chain or star configuration (see Figure B.1).

The configuration for the resistivity measurement setup is shown in Figure 2.6 which used a 24 pin GPIB cable for communication. There are eight data pins (1-4 and 13-16), three are handshake pins (6-8), and five management lines (9-11, 15 and 17) (see Figure B.2).

The communication is based on talkers/listeners. Only one device can talk at a time, and data is transfered byte per byte. The computer is a talker/listener in this setup. In a network ring, only one instrument can be the talker while the rest are listeners. When the computer requests information from an instrument, it passes the control (to be a talker) while the computer becomes the listener and receives the data one byte at a time [37]. The programming interface used was NI-488.2 .NET assembly from National
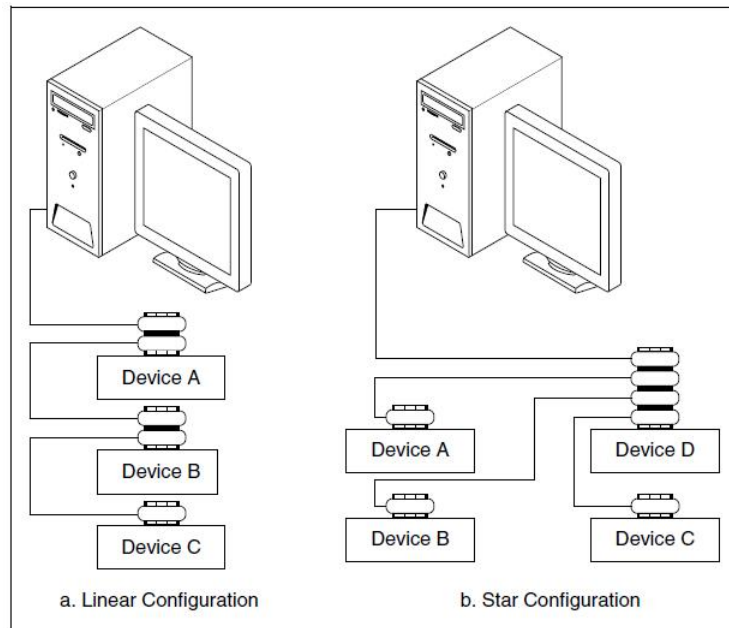
Figure B.1.: Configurations that GPIB can take on. a) Linear configuration also known as daisy chain configuration. b) Star configuration. Reproduced from [37]
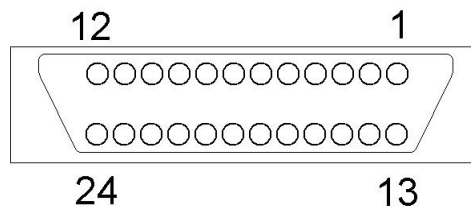
Figure B.2.: GPIB female connector with pins numbered.

Instruments. This assembly takes care of the detailed communication protocol in an easy to use API. IEEE-488 instruments have standard commands as well as vender specific commands.

Standard commands must be recognized by every IEEE-488 device. Some of the important commands used in debugging are listed in Table B.1. Devices require a unique device number ID, a number between 0 and 30, where the primary address (used

Instruction	Description
*IDN?	Returns Device Description
*RST	Resets the device
*STB?	Reads the status byte
*CLS	Clear the status

Table B.1.: Standard commands recognized by all IEEE-488 devices.

by the computer in this case) is zero. Other instruments can change their ID either by switches on the back of the device or programmatically on the front panel.

C. Program Interface

In order to handle the measurement and debugging in an efficient manner, a program was made with an extensive easy to use user interface. It was programmed in C# utilizing the NI-488.2 .NET assembly provided by National Instruments. The main form includes a dynamic graphing area where multiple graphs can be displayed simultaneously. Parameters of the experiment including the mass of the samples, how many samples to measure, applied current, what environment parameters to measure, and averaging interval are input on a side panel. This readily records directly the resistivity of the material. All data collected are saved in the specified *.dat file, which can be selected with the save file dialog. A screen shot of the program displaying some data is shown in Figure C.1.

The graphing function allows up to five graphs to be displayed at once. Zooming and auto-scaling are included in the program, which makes it convenient to look at old data from other experiments.

When sample contacts break during an experiment, or if some connection is broken, sometimes it is unknown to the operator and can be difficult to locate the source of the
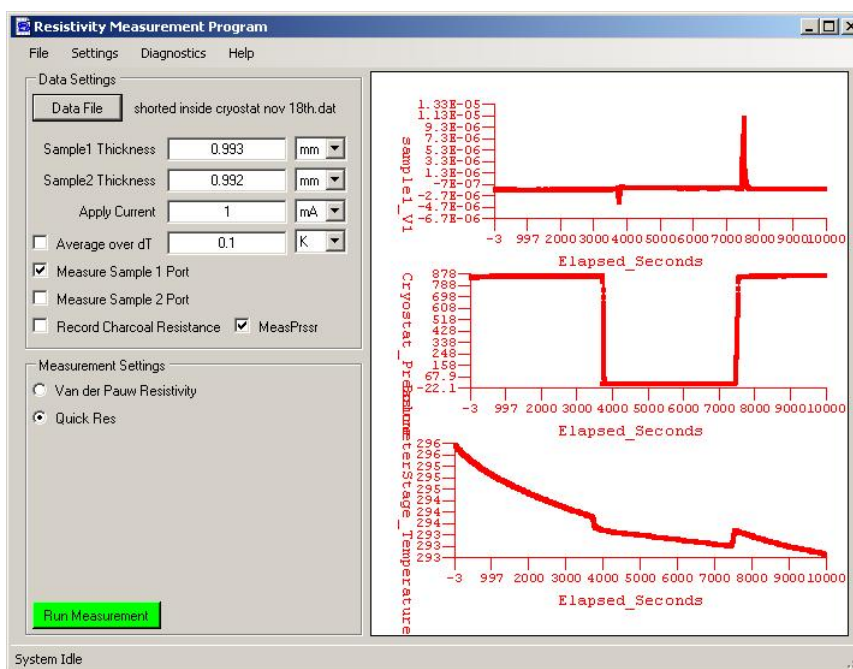
Figure C.1.: A screen shot of the resistivity measurement system program main form. Right Panel is the graphing area, upper left panel is the experiment parameters, and lower left is the type of measurement to perform.

problem. A debugging form was programmed to discover where the source of problems may be located. It shows (see Figure C.2) the circuit diagram of the circuit constructed in the HP 34903A switch card showing the current state of each relay there within. The cross settings buttons configure a Hall effect configuration, but also can debug improper configuration of the contacts on the sample. Checking the voltage reading when current is on vs. off makes a very quick determination of whether a contact has broken or not.

Each instrument has its own vender specific instruction set. To keep the program versatile, it was programmed with .net interfaces so that different instruments could be used with minimal programming. Only a few lines of code is necessary to construct a
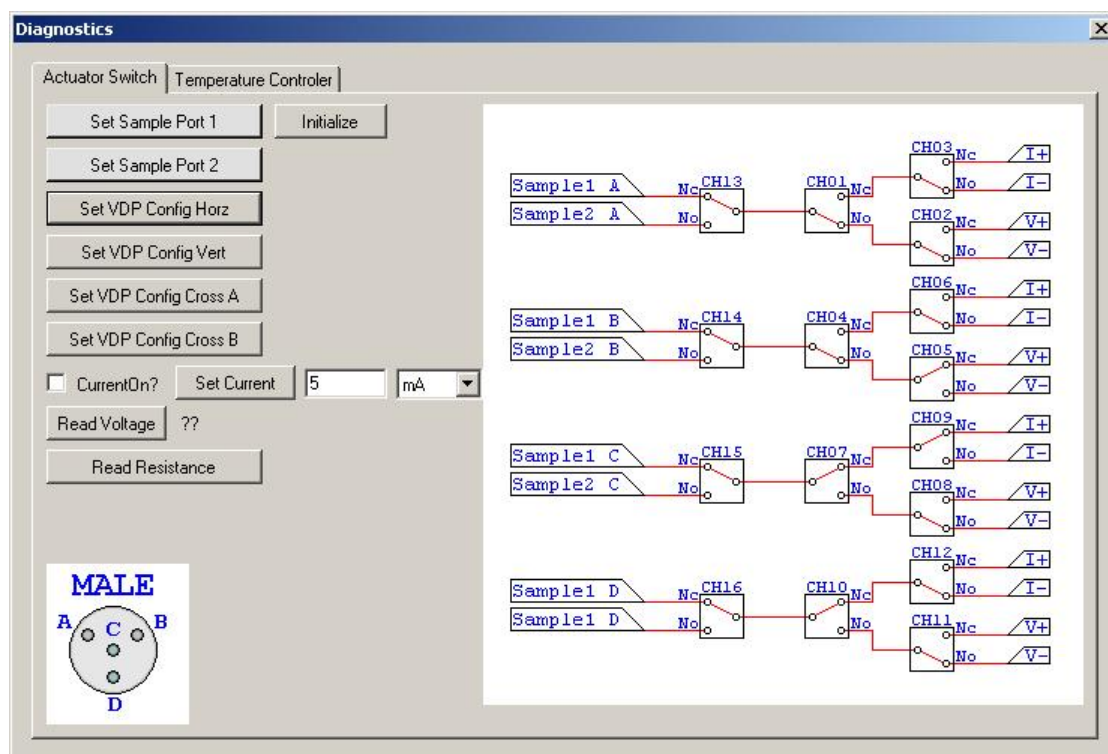
66

Figure C.2.: A screen shot of the resistivity measurement system program diagnostics screen. The tab that is selected shows a diagram of the circuit inside the HP 34903A switch card as well and multiple commands to diagnose the source of a problem.

new set of commands that the program can use to perform measurements. Changing the instruction set involves just selecting a different instrument from the drop down list (see Figure C.3).

Data is saved as a text file with the first row as the column names separated by commas. This format is easily accepted into Microsoft Excel, Igor Pro or Origin for further data analysis.
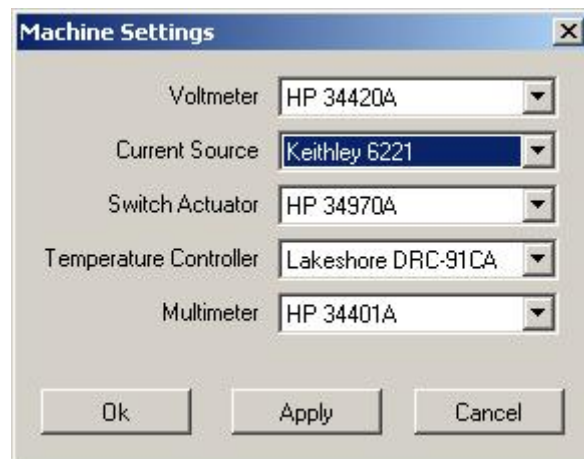
Figure C.3.: A screenshot of the resistivity measurement system program machine settings screen. Instruments may be swapped out or replaced, while the program can still operate.

Bibliography

[1] J. Bardeen, L. N. Cooper, and J. R. Schrieffer *Theory of Superconductivity*, Phys. Rev. 108, 1175, 1957.

[2] H. Frölich *On the Theory of Superconductivity: One Dimensional Case*, Proceedings of the Royal Society A. 223 (1154):296-305, 1954.

[3] George Grüner, *Charge Density Waves In Solids* Perseus Publishing, Cambridge Massachusetts, 1994

[4] J.A. Wilson, F.J. Di Salvo and S. Mahajan *Charge-Density Waves in Metallic, Layered, Transition-Metal Dichalcogenides*, Phys. Rev. L 32, 882 April 1974.

[5] E. Morosan et al, *Superconductivity in CuxTiSe2*, Nature Physics Vol 2 pg 544, Aug 2006.

[6] D. W. Shen, B.P. Xie, J.F. Zhao, Et al. *Novel Mechanism of a Charge Density Wave in a Transition Metal Dichalcogenide* Phys Rev L 99, 216404, 2007.

[7] T. Yokoyaet al., *Fermi Surface Sheet-Dependent Superconductivity in 2H-NbSe$_2$* Science 294, 2518, 2001.

[8] G. Wu H. X. Et al, *Transport properties of single-crystaline CuxTiSe2* Phys Rev B 76, 024513, 2007.

[9] S. S. Jaswal *Lattice dynamics of TiSe$_2$* Phys Rev B 20, 5297, 1979.

[10] L. J. van der Pauw *A Method of Measuring Specific Resistivity and Hall Effect of Discs of Arbitrary Shape* Philips Res. Repts. 13, 1-9, 1958.

[11] L. J. van der Pauw *A Method of Measuring The Resistivity and Hall Effect on Lamellae of Arbitrary Shape* Philips Res. Repts. 20, 220-224, 1958.

[12] J. B. Johnson *Thermal Agitation of Electricity in Conductors* Phys. Rev. 32, 97, 1928.

[13] Noëlle Pottier, *Nonequilibrium Statistical Physics, Linear Irreversible Processes* Oxford University Press, New York, 2010.

[14] H. Nyquist *Thermal Agitation of Electric Charge in Conductors* Phys. Rev. 32, 110, 1928.

[15] Supriyo Data *Lessons from Nanoelectronics, A New Prospective on Transport* World Scientific, 2012.

[16] Constantine A. Balanis, *Antenna Theory* Second Edition, Wiley, Sheel Print-N-Pack Noida, India, 2009.

[17] Magnetic Shield Corp., *Fabrication with MuMetal* Brochure, 2012.

[18] Jason Iwachow, *1/F Noise in Josephson Junctions* Undergraduate Thesis, University of Waterloo, January 17 2011.

[19] *HDL-10 Cryostat* IR Labs, 1995.

[20] David J. Griffiths, *Introduction to Electrodynamics* Third Edition, Pearson Addison Wesley, Prentice-Hall Inc., 1999.

[21] Charles Kittel, *Introduction to Solid State Physics* Eighth Edition, Wiley, 2005.

[22] *HP 34420A Nano Volt Micro Ohm Meter User's Guide* Hewlett Packard, Printed in the USA, 1994.

[23] F. London, H. London, *The Electromagnetic Equations of the Supraconductor*, Proceedings of the Royal Society A. 149 (866):71, 1935.

[24] A. B. Pippard, *An Experimentaland Theoretical Study of the Relation between Magnetic Field and Current in a Superconductor*, Proceedings of the Royal Society A. 216 (1127):547-568, 1953.

[25] M. Tinkham, *Introduction to Superconductivity* Second Edition, McGraw-Hill Inc., 1996.

[26] Charles P. Poole Jr. *Handbook of Superconductivity* Academic Press, 2000

[27] Harold T. Stokes *Solid State Physics* Allyn and Bacon Inc., 1987.

[28] James F. Annett *Superconductivity, Superfluids and Condensates* Oxford University Press, 2004.

[29] L. N. Bulaevskii, *Inhomogeneous state and the anisotropy of the upper layer critical field in layered superconductors with josephson layer interaction*, Sov. Phys. JETP, 38:634, 1974.

[30] Elisabeth J. Nicol *Pair-Breaking in Superconductivity* McMaster University, 1991.

[31] P. Flude *Cooper Pair Breaking*, Mod. Phys. Lett. B 24, 26:2601-2624 2010.

[32] Neil W. Ashcroft, N. David Mermin, *Solid State Physics* Brookes/Cole, 1976.

[33] W. Kohn *Image of the Fermi Surface in the Vibration Spectrum of a Metal*, Phys. Rev. Lett. 2, 393, 1959.

[34] Mike McElfresh *Fundamental of Magnetism and Magnetic Measurements Featuring Quantum Design's Magnetic Property Measurement System* Quantum Design Inc., 1994.

[35] Li G. et al, *Anomalous Metallic State of Cu0:07TiSe2: An Optical Spectroscopy Study*, Phys. Rev. Lett. 99, 167002, 2007.

[36] R.C. Morris, *Connection between Charge-Density Waves and Superconductivity in $NbSe_2$*, Phys. Rev. Lett. 34, 1164, 1975.

[37] *NI-488.2 User Manual* National Instruments, February 2005.